

# Adaptive Uncertainty-Guided Surrogates for Efficient phase field Modeling of Dendritic Solidification

Eider Garate-Perez<sup>1,2,\*</sup>, Kerman López de Calle-Etxabe<sup>1</sup>, Oihana Garcia<sup>1</sup>,  
Borja Calvo<sup>3</sup>, Meritxell Gómez-Omella<sup>1</sup>, and Jon Lambarri<sup>4</sup>

<sup>1</sup>Intelligent Information Systems, Tekniker, Iñaki Goenaga 5, Eibar (20600) Spain

<sup>2</sup>Faculty of Informatics UPV-EHU, Paseo Manuel de Lardizabal 1, Donostia (20700) Spain

<sup>3</sup>Department of Computer Sciences and Artificial Intelligence, UPV-EHU, Donostia (20700)  
Spain

<sup>4</sup>Advanced Manufacturing Technologies, Tekniker, Iñaki Goenaga 5, Eibar (20600) Spain

\*Corresponding author. [eider.garate@tekniker.es](mailto:eider.garate@tekniker.es)

## Abstract

The high computational cost of phase field simulations remains a major limitation for predicting dendritic solidification in metals, particularly in additive manufacturing, where microstructural control is critical. This work presents a surrogate model for dendritic solidification that employs uncertainty-driven adaptive sampling with XGBoost and CNNs, including a self-supervised strategy, to efficiently approximate the spatio-temporal evolution while reducing costly phase field simulations. The proposed adaptive strategy leverages model uncertainty, approximated via Monte Carlo dropout for CNNs and bagging for XGBoost, to identify high-uncertainty regions where new samples are generated locally within hyperspheres, progressively refining the spatio-temporal design space and achieving accurate predictions with significantly fewer phase field simulations than an Optimal Latin Hypercube Sampling optimized via discrete Particle Swarm Optimization (OLHS-PSO). The framework systematically investigates how temporal instance selection, adaptive sampling, and the choice between domain-informed and data-driven surrogates affect spatio-temporal model performance. Evaluation considers not only computational cost but also the number of expensive phase field simulations, surrogate accuracy, and associated  $CO_2$  emissions, providing a comprehensive assessment of model performance as well as their related environmental impact.

**Keywords:** adaptive sampling, surrogate model, phase field, additive manufacturing, dendritic solidification, spatio-temporal modeling.

# 1. Introduction

The ecological awareness that has emerged in recent decades has reshaped manufacturing, prioritizing durability, sustainable materials, and production processes that reduce energy consumption and waste, while emphasizing recyclability and reusability (Jarfors et al., 2024; Panagiotopoulou et al., 2022). To this transformation is added the other design conflicts that until now were found in manufacturing: improving the physical properties of the materials and maximizing the economic performance of the products (Fassi & Aniyou, 2023). This convergence highlights the importance of designing products that simultaneously meet ecological, functional, and economic requirements.

In this context, computational models offer a significant advantage by capturing the underlying physical relationships of the phenomena involved (J. Wang et al., 2022), avoiding unnecessary material waste and reducing the associated economic costs (Nyamekye et al., 2024). This approach not only accelerates innovation but also aligns with sustainable practices.

However, traditional and accurate physical models capable of simulating the properties associated with a design are often computationally expensive, particularly when searching for optimal configurations across large design spaces (Duquesnoy et al., 2023; Würth et al., 2023; Xue et al., 2024). Artificial Intelligence (AI) and Machine Learning (ML) have emerged as powerful alternatives to complex simulations, offering the ability to rapidly and reliably predict material properties (Usman et al., 2024; J. Wang et al., 2022). This more efficient prediction enables the optimization of design problems that would otherwise be prohibitive when relying solely on conventional computational models.

This approach, commonly termed a surrogate model (Azarhoosh & Ilchi Ghazaan, 2025; Kaminsky et al., 2021; Ravutla et al., 2025), aims to replace complex computational models or experiments with ML approximations that minimize accuracy loss while enabling optimization, design exploration, and performance improvement at manageable computational cost (Khatouri et al., 2022). Surrogate models are generally trained on reduced datasets that capture the essential characteristics of the phenomenon, generated either by the original model or derived from experimental data (Forrester & Keane, 2009). The construction of such datasets, known as sampling (Di Fiore et al., 2024), is critical to ensuring representativeness while avoiding excessive computational expense.

In the literature, two main sampling strategies are distinguished: classical sampling, which is performed at the initial stage when limited information about the phenomenon is available, and therefore focuses on ensuring adequate exploration of the design space; and adaptive sampling, which iteratively integrates with surrogate model training to exploit model information and thereby enhance both exploration and exploitation of the space (Herten et al., 2017; H. Liu et al., 2018; Samadian et al., 2025). Many studies have shown that adaptive sampling is able to achieve more accurate surrogate models with less data than classical sampling, and therefore, the training of these is more efficient with

particularly expensive models or experiments (Viana et al., 2021). 71

Building on these advances, it becomes possible to address domain-specific challenges 72 that traditionally rely on expensive simulations. One such challenge is the prediction of 73 dendritic solidification geometries in metals, a complex phenomenon whose accurate mod- 74 eling is computationally demanding (Bhagat & Rudraraju, 2023). These microstructural 75 patterns are directly linked to the physical and mechanical properties of the solidified 76 material (Kurz et al., 2021), and their accurate characterization is essential for ensuring 77 the performance of the final component. The importance of this problem is intensified in 78 additive manufacturing (AM), where metals undergo rapid solidification processes that 79 critically determine the reliability of the produced parts (Yu et al., 2022). AM technolo- 80 gies, recognized for their precision, reduced material waste, and environmental advantages 81 (Javaid et al., 2021; Jiang et al., 2022), require models capable of capturing solidification 82 phenomena to align with both ecological and functional demands. 83

Among the computational approaches employed to address this challenge, the phase 84 field model stands out as one of the most widely used (Dobracev et al., 2023; Tang & Du, 85 2022; Zeng et al., 2024). This method enables the simulation of dendritic solidification 86 geometries in 1D, 2D, or 3D, providing a detailed description of microstructural evolution 87 during solidification (Ji et al., 2025; S. Mao et al., 2024; Seiz et al., 2023). Although higher- 88 dimensional phase field models yield greater accuracy in simulating dendritic solidification, 89 they also entail a steep increase in computational cost. In additive manufacturing, this 90 makes surrogate models particularly valuable, as they approximate phase field behavior 91 with far lower computational demand (Choi et al., 2024; Lee & Kim, 2023; Viardin et 92 al., 2025). In this context, adaptive sampling is crucial for efficient surrogate modeling. 93 By guiding data acquisition based on model predictions, it reduces the computational 94 cost of high-fidelity simulations while ensuring that key features of dendritic solidification 95 are accurately captured. Nevertheless, these approaches still rely on an initial dataset 96 generated by the phase field model. Together, this strategy enables the construction of 97 precise surrogate models with fewer simulations, balancing accuracy and efficiency in the 98 exploration of solidification processes. 99

One of the biggest challenges when replacing phase field models is dealing with their 100 inherent spatio-temporal nature (Lavinias et al., 2024; Migdady et al., 2025). Most of 101 the literature focuses on using several temporal instances to predict the final stage of 102 solidification, as well as other properties related to the evolution of the microstructure. 103 For that reason, the challenge lies in accurately capturing both the temporal progression 104 and the spatial complexity of the system while minimizing reliance on the original phase 105 field model during training and prediction. 106

In the literature, different strategies have been proposed to address the spatio-temporal 107 complexity of phase field simulations. For instance, Montes De Oca Zapiain et al., 2021 108 employs the first 80 temporal instances to predict the last 5, applying a two-point statist- 109 ics transformation followed by PCA and an LSTM to estimate the final microstructure. 110

Peivaste et al., 2022 predicts subsequent instances using an encoder–decoder (U-net) architecture, while Yan et al., 2024 combines PCA, autoencoders, and LSTM networks to infer the final state from 50 instances. Similarly, Ahmad et al., 2023 investigates the number of temporal instances required to predict the final microstructure using a convolutional neural network coupled with LSTM layers. Although these approaches successfully reduce the temporal dimensionality of the problem, they still rely on phase field simulations to generate the predictor instances. Consequently, the choice and number of temporal snapshots become critical, as they directly determine the computational cost and efficiency of the overall framework. This highlights the need for strategies that not only learn from reduced temporal information but also minimize dependence on high-fidelity simulations when constructing predictive models.

In this framework, surrogate models play a central role in capturing the spatio-temporal correlations inherent to phase field simulations while alleviating their computational burden. Consequently, the selection of predictive instances becomes a critical design decision, as it directly affects model accuracy, complexity, and convergence, while also determining the degree to which dependence on the high-fidelity simulator can be reduced. When instances must be generated by the real physical model up to a time  $t_f$ , computational savings are restricted to the interval between  $t_f$  and the final solidification stage.

Beyond these key aspects, it is also essential to evaluate whether surrogate models truly deliver efficiency in a broader sense. When proposing such models to design more effective manufacturing processes—whether to enhance functionality, reduce economic costs, or mitigate environmental impact—it becomes crucial to measure and compare their performance against sustainability constraints.

The present work introduces an adaptive sampling methodology to train a surrogate model for dendritic solidification in metals, with a focus on additive manufacturing. Three main objectives guide this study: (i) to analyze the effect of temporal training instance selection on model performance, training cost, and potential computational savings relative to the original phase field simulations; (ii) to propose and compare two sampling strategies, one classical based on Optimal Latin Hypercube Sampling optimized via Particle Swarm Optimization, and one adaptive guided by model uncertainty, to assess whether adaptive sampling reduces the number of required samples while improving performance and overall training efficiency; and (iii) to evaluate two feature extraction approaches, a domain-knowledge-informed transformation coupled with XGBoost and a convolutional neural network (CNN), to compare generalization capabilities in the absence of domain knowledge against convergence and training cost. Furthermore, all analyses are conducted from a sustainability perspective, quantifying the  $CO_2$  emissions associated with each approach.

The remainder of this paper is organized as follows. Section 2, methods section, describes the phase-field modeling framework, data generation process, surrogate modeling

approaches, sampling strategies, and experimental setup. Section 3, results and discussion section, presents the evaluation of computational cost,  $CO_2$  emissions, and predictive performance, together with a discussion of the findings. Finally, Section 4, conclusions section, summarizes the main outcomes and implications of the study.

## 2. Methods

### 2.1 Phase field model for dendritic solidification in metals

The geometry of the solidification microstructure in metals plays a critical role in manufacturing processes due to its strong influence on the resulting mechanical properties. Among the manufacturing processes in which microstructure is studied are casting, welding, and additive manufacturing. These are typically the initial steps in complex process chains, and the quality of the resulting materials has a direct impact on the final products. In materials science, the complexity of solidification processes is studied across multiple scales, from the atomic to the macroscopic. In general, solidification involves complex interactions between thermal, mechanical, and chemical phenomena.

*Phase field* model is one of the most widely used and effective methodologies for studying, approximating, and simulating materials microstructural evolution. This model is capable of predicting complex, random geometries within continuous field (Tourret et al., 2022). Phase Field methods employ an order parameter, hereafter denoted as  $OP$  or  $\varphi$ , which can take values in the range  $\varphi \in [-1, 1]$  or  $\varphi \in [0, 1]$ . The intermediate values between the interval extremes represent the interface between two distinct physical states of the system: liquid and solid.

*Phase field model* is a numerical method capable of simulating microstructural evolution. As with many other numerical methods, solving the physical differential equations governing solidification processes requires significant computational cost. When large parameter spaces are to be explored, the use of the model can become computationally prohibitive (Alizadeh et al., 2020).

The model analyzed in this work simulates two-dimensional solidification with dendritic geometries characteristic of metal solidification (Biner, 2017). This simplified model does not account for phenomena resulting from fluid dynamics, phase transition-induced expansion or shrinkage, nor thermal noise. The microstructural evolution is described through the temporal changes of a non-conserved order parameter, as well as spatial variations in temperature across the domain.

Systems evolution is described by the Allen-Cahn equation,

$$\tau \frac{\partial \varphi}{\partial t} = -\frac{\delta F}{\delta \varphi}, \quad (1)$$

where  $\tau$  is the characteristic time scale. The term on the right-hand side of the equation denotes the functional derivative of Ginzburg-Landau free energy, which is defined by,

$$F(\varphi, m) = \int_V \frac{1}{2} \varepsilon^2 |\nabla \varphi|^2 + f(\varphi, m) dv, \quad (2)$$

where  $f(\varphi)$ ,  $m$  is the density of the local free energy. In this work,  $f(\varphi, m)$  is defined 186  
by a double-well potential, in such a way that it has two stable states or local minima, 187  
located at  $\varphi = 0$  and  $\varphi = 1$ , Thus,  $f(\varphi, m)$  is defined in the following way, 188

$$f(\varphi, m) = \frac{1}{4} \varphi^4 - \left( \frac{1}{2} - \frac{1}{3} m \right) \varphi^3 + \left( \frac{1}{4} - \frac{1}{2} m \right) \varphi^2. \quad (3)$$

. 189  
The  $\varepsilon$  parameter describes the thickness of the interface. Anisotropy is related to  $\varepsilon$  190  
and depends on the the outward-pointing normal vector of the interface. In particular, 191

$$\varepsilon = \bar{\varepsilon} \sigma(\theta), \quad (4)$$

where  $\bar{\varepsilon}$  defines the mean value of  $\varepsilon$  and the anisotropy  $\sigma(\theta)$  is expressed as 192

$$\sigma(\theta) = 1 + \delta \cos(j(\theta - \theta_o)). \quad (5)$$

Anisotropy is related to the degree of symmetry observed in the resulting dendritic 193  
crystals. For example, when  $j = 4$ , cubic symmetry is obtained, and when  $j = 6$ , 194  
hexagonal symmetry arises. The parameter  $\delta$  in Equation 5 defines the strength of the 195  
anisotropy. The variable  $\theta$  represents the angle relative to a reference direction, as de- 196  
scribed in Equation 6, while  $\theta_0$  denotes the initial orientation angle (Dantzig & Rappaz, 197  
2009). 198

$$\theta = \tan^{-1} \left( \frac{\partial \varphi / \partial y}{\partial \varphi / \partial x} \right) \quad (6)$$

In Equation 3, the parameter  $m$  defines the thermodynamic driving force. As the melt 199  
becomes undercooled, the well tilts toward the solid phase, causing the order parameter to 200  
shift in that direction. The value of  $m$  is defined as a function of temperature as follows: 201

$$m(T) = \left( \frac{\alpha}{\pi} \right) \tan^{-1} [\gamma (T_{eq} - T)] \quad (7)$$

where  $\alpha$  is a positive constant satisfying  $\alpha < 1$  (Kobayashi, 1993). The  $T_{eq}$  value 202  
of Equation 7 is the equilibrium temperature. Considering the explicit form of the local 203  
energy density, it is possible to obtain the evolution of the order parameter in the following 204  
way: 205

$$\tau \frac{\partial \varphi}{\partial t} = \frac{\partial}{\partial y} \left( \varepsilon \frac{\partial \varepsilon}{\partial \theta} \frac{\partial \varphi}{\partial x} \right) - \frac{\partial}{\partial x} \left( \varepsilon \frac{\partial \varepsilon}{\partial \theta} \frac{\partial \varphi}{\partial y} \right) + \nabla \cdot (\varepsilon^2 \nabla \varphi) + \varphi(1 - \varphi) \left( \varphi - \frac{1}{2} + m \right). \quad (8)$$

Finally, the evolution of the normalized temperature is defined as follows: 206

$$\frac{\partial T}{\partial t} = \nabla^2 T + \kappa \frac{\partial \varphi}{\partial t}. \quad (9)$$

From Equation 9, it can be inferred that the equilibrium temperature is 1. The parameter  $\kappa$  defines the diffusion constant, which is assumed to have the same value both the liquid and solid phases.

## 2.2 Phase field data

As previously described, the physical model is governed by seven parameters that define the thermophysical conditions of the dendritic solidification. Each specific combination of these parameters leads to a distinct dendritic solidification pattern associated with a given metal under well-defined processing conditions. Table 1 summarizes the parameters and their corresponding admissible ranges considered in this study.

Parameter	Definition	Min value	Max value
$\tau$	Characteristic time scale	$1.72 \cdot 10^{-4}$	$6 \cdot 10^{-4}$
$\varepsilon$	Interface thickness	0.005	$1.95 \cdot 10^{-2}$
$\kappa$	Diffusion constant	1	3.6
$\delta$	Related to anisotropy	0.001	0.04
$j$	Dendritic symmetry	4	6
$\alpha$	Constant related to thermodynamic driving force	0.4	0.9
$\theta_0$	Initial orientation	0.1	0.4

Table 1: Minimum and maximum feasible values for each physical model in the phase-field model.

For each admissible combination of the seven parameters, a full spatio-temporal simulation of the dendritic solidification process is performed. The spatial domain is discretized into a uniform grid of  $100 \times 100$  cells, while the temporal evolution is resolved over 4000 discrete time steps. Consequently, at each time step, the phase-field model produces two matrices of size  $100 \times 100$ : one corresponding to the temperature field and the other to the phase (solidification) field. These outputs can equivalently be interpreted as two-channel images of size  $100 \times 100$  pixels.

The objective of the surrogate modeling strategy is to predict the final solidification geometry at  $t = 4000$  from partial spatio-temporal information generated by the physical phase-field model. By replacing the full phase-field simulation with a trained artificial intelligence model, a significant reduction in computational cost can be achieved.

However, this task is non-trivial. Let  $t_f$  denote the last temporal instance provided as input to the surrogate model. When  $t_f$  is closer to  $t = 4000$ , the prediction accuracy is expected to improve, since the solidification geometry at  $t_f$  more closely resembles the final state. Nevertheless, this choice implies that only the computational cost associated with the simulation interval  $[t_f, 4000]$  is saved. Conversely, selecting a smaller  $t_f$  increases the potential computational savings but makes the prediction task more challenging.

Therefore, the selection of  $t_f$  must be carefully balanced. An appropriate choice should ensure sufficient predictive accuracy while maximizing computational savings with respect to the full phase-field simulation. In addition, minimizing the number of training samples required to reach a satisfactory level of accuracy remains a primary objective, as it directly impacts the overall efficiency of the surrogate modeling approach.

## 2.3 Surrogate Models

As mentioned, when the *Phase field* model is surrogated, the greatest difficulty lies in approximating the spatio-temporal nature of the problem.

Several proposals have been made in the literature to address such problems. For example, the work by (Montes De Oca Zapiain et al., 2021) extracts the spatial characteristics of the problem using statistical methods and dimensionality reduction techniques. To approximate the temporal relationship between images and predict the final state, it employs an LSTM (Long Short-Term Memory), which is a type of recurrent neural network. The study by (Herman et al., 2020) follows a similar methodology for describing spatial features but then uses polynomial chaos for regression and final state prediction. In contrast, the work by (Peivaste et al., 2022) uses a U-Net neural network to learn spatial features and predict the final state.

The studies by (Li et al., 2024) and (Goswami et al., 2020) propose a neural network that incorporates physical information (Physics-Informed Neural Network, or PiNN). Although the former presents the approach for a 1D *Phase field* model, it also explains the necessary modifications to apply it to 2D and 3D problems and how to use spatial data in the neural network. The later, on the other hand, is used to predict fracture geometry and specifically solves a 2D problem.

The work by (Yan et al., 2024) extracts spatial information using an autoencoder, and then approximates the temporal relationship between images using an LSTM. Similarly, (Vasylenko et al., 2021) also proposes autoencoders to automatically learn the characteristics of the images.

As mentioned in the introduction, other works have proposed neural networks capable of learning both spatial and temporal relationships simultaneously Ahmad et al., 2023. Finally, there are also proposals that incorporate information from the differential equations of the *Phase field* model into the neural networks themselves Goswami et al., 2020.

One of the main hypotheses of this work is that, although CNN models are capable of learning complex spatial problems without prior information, training such models may require a large amount of data in order to adjust all the model parameters effectively.

However, if prior knowledge about the problem is available, through proper extraction of spatial features, the problem can be approximated using a simpler surrogate model, which requires fewer data to converge.

In a context where data generation is expensive, defining surrogate models that can be

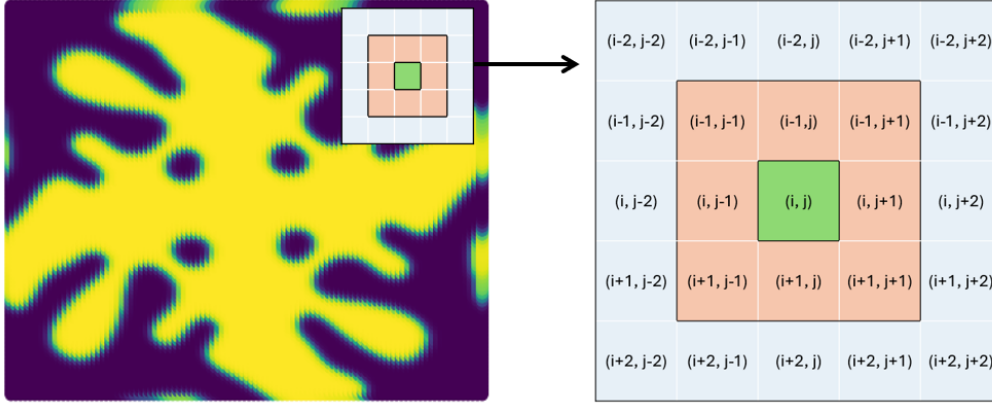


Figure 1: Extracted spatial features for the XGBoost model and for  $(i, j)$  pixel.

efficiently trained is essential. Therefore, the following modeling approaches are proposed: 272

1. **Spatial Features + XGBoost:** The spatial features of the images are extracted 273  
using statistical methods. These features are then used to train an XGBoost model, 274  
which leverages the spatial characteristics of the input images to predict the final 275  
solidification state. 276
2. **Convolutional Neural Network (CNN):** The convolutional neural network uses 277  
convolutional layers to automatically learn the spatial features of the input images. 278  
These learned features are then used to predict the final solidification state. 279
3. **Self-supervised Convolutional Neural Network:** In this method, the neural 280  
network is pre-trained using a variational autoencoder. The autoencoder learns to 281  
reconstruct images based on their features by first distorting the input images used 282  
for training. The convolutional layers of the autoencoder are the same as those used 283  
in the CNN model. During CNN training, the convolutional layer parameters are 284  
initialized with the pre-trained weights from the autoencoder. The goal in this case 285  
is to leverage the image representations learned by the autoencoder. 286

### 2.3.1 XGBoost surrogate 287

#### Spatial features extraction 288

For each image used to predict the final solidification state, spatial features are extracted. 289  
For each cell  $(i, j)$  in the image, the spatial features consist of the values of the order para- 290  
meter and temperature within a radius of  $r = 2$  around that cell. Figure 1 schematically 291  
illustrates the extraction of pixel features used for each  $(i, j)$  cell. 292

For each pixel  $(i, j)$  and a radius of  $r = 2$ , as shown in Figure 1, the values of tem- 293  
perature and order parameter from the 24 neighboring pixels are used, in addition to 294  
the values at  $(i, j)$ . Therefore, if  $n_t$  time steps or images are used to predict the final 295  
solidification state, there will be  $2 \cdot 25$  spatial features per pixel, resulting in a total of 296  
 $2 \cdot 25 \cdot n_t$  spatial features for the regression problem. 297

In addition to the spatial features, the values of the physical simulation parameters 298  
from the physical model are also included. 299

### Symmetry simplification 300

To reduce the complexity of the regression problem solved using XGBoost, the symmet- 302  
ries of the dendritic geometries are exploited. As explained earlier, this work analyzes 303  
dendrites with different anisotropy levels, exhibiting 4-fold and 6-fold symmetry patterns. 304  
Following symmetries can be identified: 305

- **Anisotropy with 4-fold symmetry:** 306

In this case, the dendritic geometry exhibits symmetry with respect to the axes 307  
 $x = 0$  and  $y = 0$ . Therefore, considering the quadrant defined by the cell range 308  
 $0 \leq i \leq 50$  and  $0 \leq j \leq 50$  as the reference, the full image can be reconstructed 309  
by applying rotations of  $90^\circ$ ,  $180^\circ$ , and  $270^\circ$  to this quadrant. Alternatively, if only 310  
one axis of symmetry is used, the half-image defined by  $0 \leq i \leq 50$  and  $0 \leq j \leq 100$  311  
can serve as the reference, and the full image can be recovered by applying a  $180^\circ$  312  
rotation. 313

- **Anisotropy with 6-fold symmetry:** 314

In this case, the dendritic pattern exhibits rotational symmetry that repeats 6, 3, and 315  
2 times. Using the 6-fold rotational symmetry, if the region defined by  $0 \leq i \leq 50$  316  
and  $0 \leq j \leq \frac{1}{3}i + \frac{100}{3}$  is taken as the reference, the entire image can be reconstructed 317  
by applying rotations of  $60^\circ$ ,  $120^\circ$ ,  $180^\circ$ ,  $240^\circ$ , and  $300^\circ$ . Alternatively, using the 318  
3-fold symmetry and the region  $0 \leq i \leq 50$  and  $0 \leq j \leq -\frac{1}{3}i + \frac{200}{3}$  as reference, 319  
the full image can be reconstructed through  $120^\circ$  and  $240^\circ$  rotations. The 2-fold 320  
rotational symmetry case is handled in the same way as the 4-fold anisotropy case. 321

In any case, thanks to the symmetry-based simplification, the model can be trained 322  
using only parts of the image. In this way, the final solidification state of a region can be 323  
predicted using less information. Then, by applying the corresponding rotations, the full 324  
image can be reconstructed. 325

In the work described in this chapter, the 4-fold rotational symmetry simplification 326  
is used for dendrites with anisotropy 4. In contrast, for dendrites with anisotropy 6, the 327  
6-fold rotational symmetry simplification is applied. 328

### XGBoost 329

The XGBoost algorithm combines multiple tree-based estimators using bagging, and re- 330  
fines the model iteratively through boosting by focusing on samples that are more difficult 331  
to predict. 332

In this work, the XGBoost Python library is used. Regarding the algorithm's hyper- 333  
parameters, default values are used in all cases except for the learning rate, maximum 334  
depth, and number of estimators, which are set to 0.01, 5, and 200, respectively. The 335  
mean squared error is used as the loss function. 336

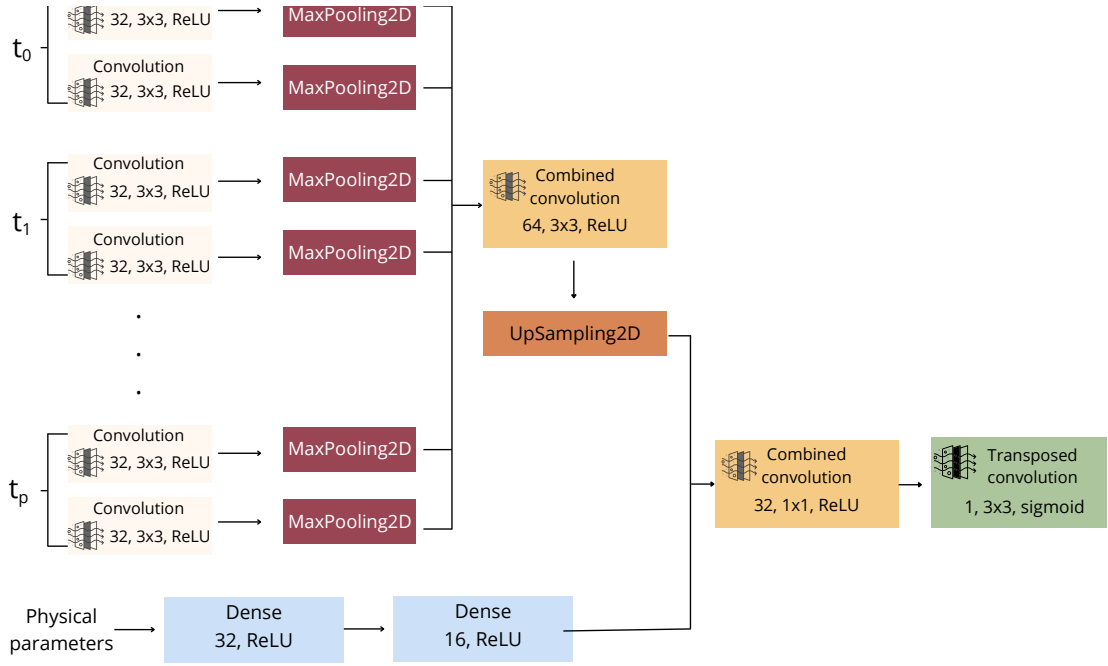


Figure 2: Architecture of the convolutional neuronal network.  $t_0, t_1, \dots, t_n$  are the training temporal instances.

### Feature Selection

For variable selection, the feature importances provided by the XGBoost model are used. To do this, all variables are ranked from most to least important, the cumulative importance is computed, and the top variables that account for up to 0.98 of the total importance are selected.

### 2.3.2 Convolutional Neural Network

The architecture of the convolutional neural network used in this work is summarized in Figure 2. The following paragraphs provide a detailed description of each component of the network.

For each training instance and for each sample, one image is generated for temperature values and another for the order parameter. The convolutional neural network applies one convolutional layer to each of these input images. Each of these layers uses 32 filters with kernel sizes of  $3 \times 3$ , which are applied with a stride of one along both spatial axes. The activation function used is ReLU (Rectified Linear Unit).

Following the convolution, the spatial dimensions of the resulting feature maps are reduced through a downsampling operation that simplifies spatial information. Specifically, max pooling is applied over non-overlapping  $2 \times 2$  regions, retaining the maximum value in each case. This reduces the image dimensions by half.

Once all the input images have passed through their respective convolutional layers, their outputs are merged through an additional convolutional layer that combines the extracted features. In this layer, 64 filters are used, with the same kernel size and parameters as in the previous layers. After this operation, the resulting feature map is upsampled to

restore the original image dimensions. 359

The physical parameters used in the simulation, the seven parameters described earlier, 360  
are integrated into the neural network. To do this, two fully connected (dense) layers are 361  
applied: the first with 32 neurons and the second with 16, both using the ReLU (Rectified 362  
Linear Unit) activation function. 363

The output from the tabular (parameter) layers is then reshaped to match the spatial 364  
scale of the image data and combined with the image features through a convolutional 365  
layer. This layer uses 32 filters with  $1 \times 1$  kernels and again applies the ReLU activation 366  
function. 367

Finally, the prediction of the output image is performed using a transposed convolu- 368  
tional layer followed by a sigmoid activation function. This final layer uses a single filter 369  
with a  $3 \times 3$  kernel and preserves the spatial dimensions of the input, enabling the network 370  
to generate a full-resolution output image. 371

To train the model, the mean absolute error (MAE) is used as the loss function, and 372  
the ADAM optimizer is employed for optimization. 373

### 2.3.3 Self-supervised Convolutional Neural Network 374

The self-supervised neural network uses the same convolutional architecture described in 375  
the previous section to predict the final solidification state. However, in this case, the 376  
convolutional layers of the neural network are pre-trained using a variational autoencoder. 377

The variational autoencoder adds noise to the input images before processing. Using 378  
the same convolutional layers as those in the main network, that is, the layers used initially 379  
to process the images, the autoencoder learns to reconstruct the original images from 380  
the noisy versions. Through this process, the autoencoder effectively learns to extract 381  
meaningful features from the images. 382

The convolutional layer parameters learned by the variational autoencoder are used 383  
to initialize the convolutional layers of the main convolutional neural network. Self- 384  
supervised learning is a methodology that has been applied to improve the training of 385  
complex neural networks when only few data is available (W. Mao et al., 2023). In the case 386  
of convolutional neural networks, which typically involve a large number of parameters, 387  
the more parameters a model has, the more data it requires to achieve accurate results. 388  
This makes properly training convolutional networks particularly challenging (Chen et al., 389  
2024). 390

When the data originates from a complex physical model, it becomes highly desirable 391  
to obtain accurate surrogate models using as little data as possible. In this context, self- 392  
supervised learning may provide an effective means to develop more efficient convolutional 393  
neural networks, particularly when used as surrogate models. 394

The architecture of the variational autoencoder used in this work is shown in Figure 3. 395  
As illustrated, temperature and order parameter images are processed separately through 396  
dedicated convolutional layers. These layers are the same ones later used in the main con- 397

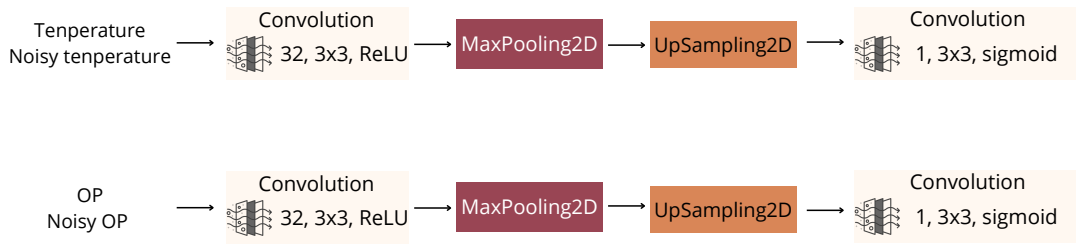


Figure 3: Architecture of the Variational Auto Encoder used in the self-supervised CNN

volutional network, each corresponding to its specific image type. After passing through 398  
 an encoding–decoding (compression and reconstruction) process, the outputs are further 399  
 processed by an additional convolutional layer. These final layers use a single filter and 400  
 apply the sigmoid activation function. The kernel size remains the same as in the initial 401  
 layers, i.e.,  $3 \times 3$ . 402

In this way, the autoencoder learns to reconstruct the original images from their noisy 403  
 versions, effectively capturing the key spatial features of the input images. As mentioned 404  
 earlier, the parameters obtained after training the first two convolutional layers are then 405  
 used to initialize the corresponding convolutional layers in the main neural network, as 406  
 shown in Figure 2. Therefore, the convolutional network begins training from a repres- 407  
 entation that already captures the predicted spatial features. 408

## 2.4 Sampling Methods 409

One of the main objectives of this work is to analyze how the sampling strategy influ- 410  
 ences the number of samples required to accurately surrogate a computationally expensive 411  
 problem such as the *Phase field* model, with the ultimate goal of minimizing the number 412  
 of simulations needed to achieve a good fit. 413

To this end, two sampling strategies are considered: classical sampling and adaptive 414  
 sampling. Classical sampling relies on an optimal Latin hypercube design, whereas the 415  
 adaptive approach incorporates new samples based on model uncertainty. The following 416  
 sections describe both methodologies in detail. 417

### 2.4.1 Classical sampling: Optimal Latin Hypercube 418

Latin Hypercube Sampling (LHS), is one of the most widely used sampling methods 419  
 in the literature (Luo et al., 2023). The technique divides the space into  $m^n$  identical 420  
 hypercubes to place  $m$  points, where  $n$  is the dimension of the space. The method 421  
 consists in distributing the  $m$  sample points so that each partition of every coordinate is 422  
 used exactly once. Specifically, if one of the  $m$  points is placed at  $(a_1, \dots, a_n)$ , and  $a_1$  lies 423

in the first cell of the  $m$ -partition along the first coordinate, then no other point is allowed to share that same cell in the first coordinate. This restriction applies to all remaining coordinates: for each  $a_i$ , no other point may occupy the same partition cell along that coordinate (McKay et al., 1979).

As is evident, for fixed values of  $n$  and  $m$ , multiple Latin Hypercube Samplings (LHS) can exist. Techniques have been proposed to select the most suitable LHS (S. Wang et al., 2019). While standard LHS ensures a certain level of point dispersion, it does not necessarily guarantee the optimal distribution. For this purpose, various methods have been developed to compute an Optimal Latin Hypercube Sampling (OLHS), which maximizes the distance among all points.

To obtain an OLHS, an optimization problem that maximizes the distance between sample points must be solved. A metric space (most commonly Euclidean) is selected, and an appropriate optimization algorithm is applied. Several methods have been proposed in the literature to generate optimal Latin hypercubes. For instance, (Borisut & Nuchitprasittichai, 2023) reviews different techniques for optimizing LHS, most of which aim to maximize inter-point distances, although some approaches also maximize entropy or incorporate other objective functions.

Classical, metaheuristic, and genetic algorithms have all been employed to solve OLHS problems. For example, in distance-maximization scenarios, Park et al., 2025 uses an evolutionary algorithm, while Aziz & Tayarani- N., 2014 employs a genetic algorithm based on Particle Swarm Optimization (PSO). Other approaches reported in the literature include simulated annealing and various adaptive evolutionary algorithms (Escobar-Cuevas et al., 2024), as well as propagation–translation LHS methods (Park et al., 2025).

In this work, a discrete Particle Swarm Optimization (PSO) approach is proposed to obtain an OLHS. In this optimization problem, each LHS represents a feasible solution. An LHS with  $m$  points, in any  $n$ -dimensional space, can be represented as a permutation of  $m$  values along each of the  $n$  coordinates. Indeed, in the space  $X_1 \times X_2 \times \dots \times X_n$ , if a point  $(a_1, \dots, a_n)$  is placed, each  $a_i$  corresponds to a cell in the LHS along coordinate  $i$ . Consequently, no other point in the sample may occupy the same LHS cell, i.e., no other point satisfies  $X_i = a_i$  for  $i = 1, \dots, n$ .

Thus, if  $m$  uniform cells are defined for each coordinate, each cell contains exactly one point. For instance, consider a two-dimensional case: for the first coordinate, each discretized cell contains a value, which simultaneously corresponds to a coordinate between 1 and  $m$  in the second dimension. The permutation positions indicate the cell in the first coordinate, while the values represent the corresponding positions in the second coordinate. More generally, in an  $n$ -dimensional sampling, if coordinates are considered in pairs and the sample is represented relative to one another across all coordinates, the LHS can be fully defined by  $n$  permutations of  $m$  values.

As an example, if we want to place 7 points in the  $[0, 1] \times [0, 1]$  space, the LHS illustrated in Figure 4 can be represented as  $\{(4, 3, 1, 2, 6, 5, 7), (3, 4, 2, 1, 6, 5, 7)\}$ .

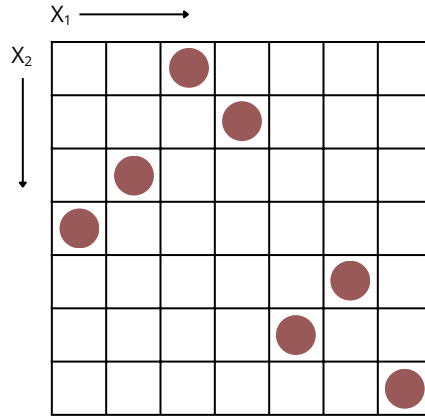


Figure 4: 7 points LHS sampling for the  $[0, 1] \times [0, 1]$  space.

The fitness value of each population is based on the Morris-Mitchell dispersion (Xiao et al., 2022). A small dispersion value represents a large distance between points. It is calculated as:

$$fitness = \left( \sum_{i=1}^m \sum_{j=i+1}^m d(p_i, p_j)^{-\delta} \right)^{1/\delta}, \quad (10)$$

where  $d(p_i, p_j)$  is the distance between the  $i$ -th and  $j$ -th points in the LHS, and  $\delta$  is a pre-defined constant. In this work, the Euclidean distance is used and  $\delta = 50$ .

Each population is transformed in every iteration using the following two techniques:

- **Move toward optimum.** The goal is to move the population toward local and global optima. For each parameter  $X_i$ , movements are performed toward both the local and global optima. The procedure follows these steps, also illustrated in Figure 5:
  1. Positions whose values will be randomly modified are selected.
  2. For each value of the first point, the variable is assigned the value of the local or global optimum at that position.
  3. The position where the particle originally held the newly assigned value is identified, and the value at that position is replaced by the value that was just moved.

The transformation is first applied toward the local optimum and then toward the global optimum. The number of positions to be changed and the specific positions are randomly selected in each case.

- **Random swap.** Two positions are randomly selected, and their values are exchanged.

Movement toward the optima is applied in every iteration, but the movement “speed,” i.e., the number of positions changed, varies for each transformation. The random swap is

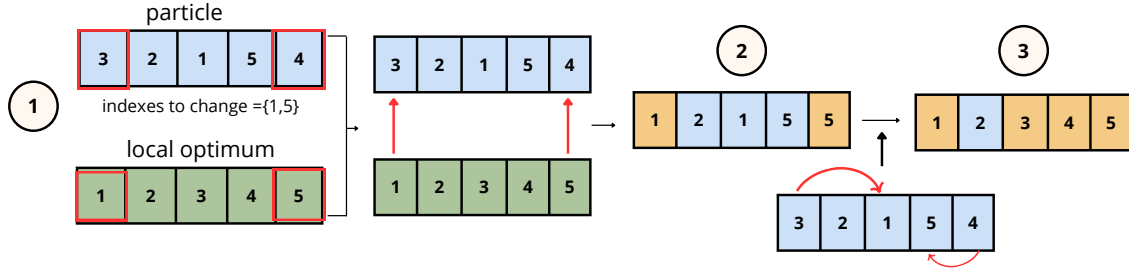


Figure 5: Transformation toward the local and global optimum. The example shows the local optimum case; the global case is symmetric.

applied probabilistically: for each variable, a value is sampled from a uniform distribution. 487  
 If this value is smaller than a pre-defined threshold  $R$ , a random swap is performed. In 488  
 this work,  $R = 0.7$  is used. 489

Finally, the new population is evaluated, and the global and local optima are updated 490  
 along with the population. The whole algorithm is defined in the pseudocode defined in 491  
 Algorithm 1. 492

## 2.4.2 Uncertainty based adaptive sampling 493

Adaptive sampling aims to iteratively improve surrogate models or optimization processes 494  
 by selecting new samples based on model performance and uncertainty. Classical sampling 495  
 strategies typically emphasize exploration only, which can be inefficient when the relation- 496  
 ship between input variables and the output is highly nonlinear and unknown. Balancing 497  
 exploration and exploitation is therefore essential for constructing accurate and efficient 498  
 adaptive sampling (Viana et al., 2021). In surrogate-based modeling, adaptive sampling 499  
 allows extracting information effectively from computationally expensive simulations as 500  
 the studied in this work (Viana et al., 2021). As the relationship between the input space 501  
 and the response is initially unknown, and because the number of samples strongly in- 502  
 fluences performance, strategies that adaptively refine the design are crucial (Lookman 503  
 et al., 2019). 504

Adaptive sampling methods address these challenges by iteratively enriching the train- 505  
 ing dataset with points that improve the model, striking a balance between exploration 506  
 and exploitation (Fuhg et al., 2021; Lookman et al., 2019). Among the most effective 507  
 strategies are those based on epistemic uncertainty estimation. These methods quantify 508  
 the predictive uncertainty of the surrogate model over the entire design space and add 509  
 samples in regions where uncertainty is highest. High-uncertainty regions can arise either 510  
 from sparse sampling (lack of exploration) or from areas with steep response gradients 511  
 (need for exploitation), even if nearby points exist (Hüllermeier & Waegeman, 2021). 512

Numerous approaches for uncertainty estimation have been proposed in the literat- 513  
 ure (Fakour et al., 2024; Heid et al., 2023), and their effectiveness is closely tied to the 514

---

**Algorithm 1** PSO for Optimal Latin Hypercube Sampling

---

**Require:**  $n\_points, n\_features, n\_pop, max\_iter, tol, distance\_method, p, R$

**Ensure:** Best LHS design and fitness history

```
1: Initialize population:
2: for particle  $i = 1$  to  $n\_pop$  do
3:   Generate random LHS of size  $(n\_points \times n\_features)$ 
4: end for
5: Compute fitness of each particle using Morris-Mitchell dispersion
6: Identify initial global best (gbest) and local best (lbest)
7: Record gbest fitness history
8: for iteration = 1 to  $max\_iter$  do
9:   if  $tol \geq tolerance\_threshold$  then
10:    break
11:   end if
12:   for particle  $i = 1$  to  $n\_pop$  do
13:     Extract current  $LHS_i$  for particle
14:     for feature  $j = 1$  to  $n\_features$  do
15:       Randomly select number of positions to move toward lbest and gbest
16:       Select indices of positions:  $same\_num\_p, same\_num\_g$ 
17:       Change particle
18:        $new\_LHS_i \leftarrow move\_design(feature_j, LHS_i, lbest, same\_num\_p)$ 
19:        $new\_LHS_i \leftarrow move\_design(feature_j, LHS_i, gbest, same\_num\_g)$ 
20:       if  $rand() < R$  then
21:          $new\_LHS_i \leftarrow rand\_swap(LHS_i, feature_j)$ 
22:       end if
23:     end for
24:   end for
25:    $new\_fitness \leftarrow compute\_fitness(new\_population, distance\_method, p, R)$ 
26:   for particle  $i = 1$  to  $n\_pop$  do
27:     if  $new\_fitness > previous\_fitness$  then
28:        $LHS_i \leftarrow new\_LHS_i$ 
29:        $fitness_i \leftarrow new\_fitness_i$ 
30:     if  $new\_fitness > gbest\ fitness$  then
31:       Update gbest
32:       Record gbest fitness
33:       Update tolerance
34:     end if
35:   end if
36: end for
37:   Update lbest to particle with maximum fitness in current population
38: end for
39: return gbest LHS and fitness history
```

---

surrogate model employed. Probabilistic models offer a more direct way to quantify uncertainty compared to deterministic ones. Nevertheless, reliable uncertainty measures for deterministic surrogates also exist. For neural networks, for example, Monte Carlo dropout provides a practical Bayesian approximation by randomly deactivating neurons during inference (Gal & Ghahramani, 2015). Other model-agnostic approaches include quantile-based loss functions, numerical methods to estimate joint conditional distributions (Tyralis & Papacharalampous, 2024), or model ensemble methods (Hoffmann et al., 2021; Rahaman & thiery alexandre, 2021).

Building on these ideas, the adaptive method proposed in this work combines exploration and exploitation through uncertainty-driven sampling. By iteratively measuring and leveraging the model’s uncertainty, new points are added in the most informative regions of the design space, enhancing both accuracy and efficiency.

### Monte Carlo Dropout for uncertainty estimation

In the case of neural networks, the *Monte Carlo dropout* method was employed to quantify uncertainty. This approach has been widely adopted to estimate epistemic uncertainty in neural networks (Z. Liu et al., 2025; Padarian et al., 2022; Zeevi et al., 2024). Moreover, as explained in (Seoh, 2020), neural networks trained and evaluated with *Monte Carlo dropout* are analogous to Bayesian neural networks and provide reliable uncertainty estimates.

*Dropout* is a regularization technique originally designed to prevent overfitting in neural networks. The method randomly deactivates a proportion of neurons and can be applied during both training and inference. In this work, dropout is applied at two stages during training: first, after each layer that processes the image data (following the structure shown on the left side of Figure 2); and second, in the convolutional layer where physical parameter features and image features are combined (the second layer from the right in Figure 2).

After training, dropout is also applied during inference, where random network connections are deactivated and ignored for prediction. For each input image, 100 stochastic forward passes are performed using dropout, resulting in 100 predictions. The mean of these predictions is taken as the final network output, while the standard deviation across the 100 predictions serves as the measure of predictive uncertainty.

To obtain a spatial distribution of the model uncertainty and an overall uncertainty estimate for each model, cross-validation is employed. All available samples are divided into 10 groups of equal size, and during 10 iterations, one group is used for validation while the remaining 9 groups are used for training. In each case, uncertainty is computed on the validation samples.

### Bagging XGBoost Trees for uncertainty estimation

For XGBoost, the methodology used combines bootstrap and bagging techniques to estimate the model’s epistemic uncertainty. Similar approaches have been described in the literature for quantifying uncertainty in tree-based machine learning models (Brophy & Lowd, 2022; Malinin et al., 2021). Although the variance induced by bootstrap resampling is not a purely epistemic measure—because subsampling of instances and features introduces additional sampling noise—it has been widely adopted as a practical approximation to epistemic uncertainty in complex regressors, as demonstrated for example in Lookman et al., 2019, Fakour et al., 2024, and Heid et al., 2023. Moreover, Palmer et al., 2022 shows that while bootstrap-based uncertainty is not an exact estimator of epistemic error, it remains strongly and monotonically correlated with the true prediction error, supporting its use as a reliable and informative approximation.

As mentioned earlier, the XGBoost implementation employed in this work uses 200 estimators. Each estimator is trained on a random subset of both features and samples. During inference, a random %75 of the trained estimators is selected for each prediction, and the prediction process is repeated 100 times per input sample. The mean value of these repetitions is taken as the final prediction, while the standard deviation across the 100 repetitions serves as the uncertainty measure.

Similar to the methodology adopted for neural networks, cross-validation is also employed here to approximate the overall uncertainty across the entire input space. In this case, %20 of the samples are randomly selected for validation, and 10 repetitions are performed. In each repetition, uncertainty is computed on the validation samples.

### Definition of new samples

Using the uncertainty estimates obtained for each model, regions of high uncertainty are identified in order to introduce new samples within those regions.

As previously mentioned, uncertainty is computed on the validation samples using the two methodologies described above. In any case, this approach only provides uncertainty values for samples that are already part of the design set. However, the use of cross-validation allows representing uncertainty across the entire input space, particularly considering that the initial sampling is performed via OLHS.

In this work, if the number of samples at iteration  $k$  is denoted as  $n_k$ , then for iteration  $k + 1$ , an additional  $\lfloor 0.15n_k \rfloor$  samples are added to the design set, resulting in  $n_{k+1} = \lfloor 1.15n_k \rfloor$  total samples. At each iteration, these  $\lfloor 0.15n_k \rfloor$  new samples are selected based on the model uncertainty as follows:

1. At iteration  $k + 1$ , the  $\lfloor 0.15n_k \rfloor$  candidate points with the highest uncertainty are identified.
2. For each of these points, the distance to all other points in the design set is computed, and the nearest neighbor is identified.

3. Hyperspheres are defined with centers at the high-uncertainty points and radius equal to half the distance computed in step 2. 592  
593
4. For each hypersphere, one new sample is randomly generated within it. This set of points constitutes the  $\lfloor 0.15n_k \rfloor$  new samples added to the design set. 594  
595

As an illustrative example, Figure 6 depicts the adaptive sampling procedure for two physical parameters at iteration  $k$ . 596  
597

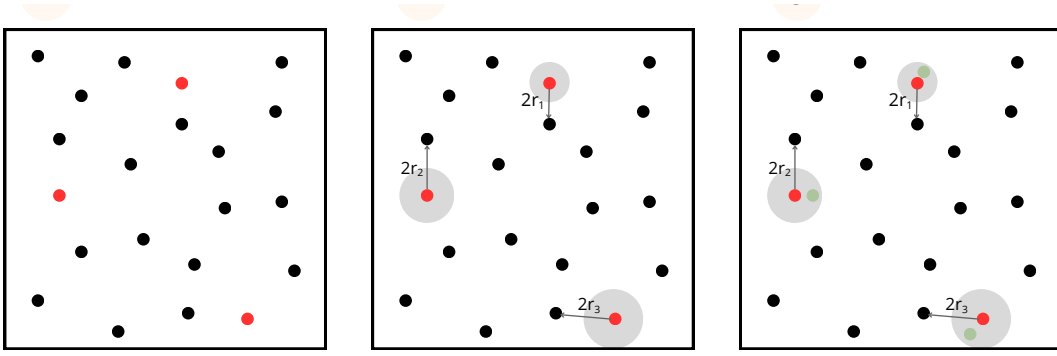


Figure 6: Definition of new samples based on uncertainty estimation. Red points denote the samples with the highest uncertainty, while green points represent those added for iteration  $k + 1$ .

### Adaptive Sampling Based on Mixed Uncertainty 598 599

The predictive uncertainty of each sample is computed from the pixel-wise uncertainty of its predicted solidification image, using the Monte Carlo Dropout and bagging strategies explained above. 600  
601  
602

Each sample or image is partitioned into three zones according to the solidification phase predicted for each pixel: pixels with values below  $\delta$  are assigned to the *liquid* zone, those above  $1 - \delta$  to the *solid* zone, and the remaining pixels to the *interface* zone (the transition between liquid and solid), where  $\delta$  is a small positive value close to 0. 603  
604  
605  
606

For each sample  $i$ , the mean uncertainty is calculated separately over each zone, denoted by  $\bar{U}_{\text{liq}}^{(i)}$ ,  $\bar{U}_{\text{int}}^{(i)}$ , and  $\bar{U}_{\text{sol}}^{(i)}$ . 607  
608

The interface region, being the most difficult to predict and determining the final geometry of the solidified metal, and consequently its mechanical properties, is assigned the largest weight when aggregating the uncertainty. The mixed uncertainty is therefore defined as: 609  
610  
611  
612

$$U_{\text{mixed}}^{(i)} = w_{\text{liq}} \bar{U}_{\text{liq}}^{(i)} + w_{\text{int}} \bar{U}_{\text{int}}^{(i)} + w_{\text{sol}} \bar{U}_{\text{sol}}^{(i)},$$

with  $w_{\text{liq}} = 0.1$ ,  $w_{\text{int}} = 0.6$ , and  $w_{\text{sol}} = 0.3$ . 613

These mixed uncertainty values are used within the adaptive sampling algorithm (Algorithm 2) to rank the samples, select those with the highest uncertainty, and generate new candidate points to enrich the design space. 614  
615  
616

---

**Algorithm 2** Adaptive Sampling Based on Mixed Uncertainty

---

**Require:**  $p, uncertainty\_df, doe, w_{liq}, w_{int}, w_{sol}, \delta$

**Ensure:** New sample points and updated DOE

- 1: Compute mixed uncertainty for all samples:
- 2: **for** each sample  $i$  in `uncertainty_df` **do**
- 3:   Partition predicted solidification image into zones:  
    liquid: pixels  $\leq \delta$ ,  
    solid: pixels  $\geq 1 - \delta$ ,  
    interface: remaining pixels
- 4:   Compute mean uncertainty per zone:  $\bar{U}_{liq}^{(i)}, \bar{U}_{int}^{(i)}, \bar{U}_{sol}^{(i)}$
- 5:   Compute mixed uncertainty:

$$U_{mixed}^{(i)} = w_{liq} \bar{U}_{liq}^{(i)} + w_{int} \bar{U}_{int}^{(i)} + w_{sol} \bar{U}_{sol}^{(i)}$$

- 6: **end for**
  - 7: Sort samples by  $U_{mixed}^{(i)}$  in descending order
  - 8: Select top  $p$  most uncertain samples: `p_most_uncertain`
  - 9: **for** each sample in `p_most_uncertain` **do**
  - 10:   Compute scaled coordinates within  $[0,1]$  range for all features
  - 11:   Find nearest existing sample and compute half-distance
  - 12:   Define hypersphere centered at sample with radius = half-distance
  - 13:   Generate new candidate point randomly inside hypersphere
  - 14:   Rescale new point back to original feature space
  - 15: **end for**
  - 16: Assign new experimental IDs to generated points
  - 17: Concatenate new points with existing DOE
  - 18: **return** new sample points, updated DOE
- 

## 2.5 Experimental setup

617

This section describes the experimental framework developed to evaluate the hypotheses presented in this work.

618  
619

### 2.5.1 Training Temporal Instances

620

For spatio-temporal problems such as phase field simulations, it is essential to capture both spatial and temporal features of the system. Spatial features are handled as described in Section 2.3.1. Temporal features require careful selection of discrete time instances used to train the surrogate model. The final state prediction is strongly influenced by the temporal instances closest to the target time.

621

622

623

624

625

The computational cost of surrogate model predictions depends on the number and choice of temporal instances simulated using the original high-fidelity model. Let  $t_f$  denote the last time instance used for training; the potential computational savings are inversely proportional to the cost of simulating the instances between the initial time and  $t_f$ . Based on this principle, three temporal instance sets are defined for evaluation:

626

627

628

629

630

- $ID_1 = \{1000, 1500, 2000, 2500\}$

631

- $ID_2 = \{1000, 1500, 2000, 2500, 3000\}$  632
- $ID_3 = \{1000, 1500, 2000, 2500, 3000, 3500\}$  633

These configurations correspond to executing approximately half, three-quarters, and seven-eighths of the full simulations required to predict  $t = 4000$  using the surrogate. 634 635

## 2.5.2 Sampling Size 636

For adaptive sampling, the initial design follows the recommendations of Fuhg, 2019; Tenne, 2015, and Afzal et al., 2017, setting the initial sample size to  $10n$ , where  $n = 7$  is the number of physical parameters, yielding 70 initial points. At each iteration  $k + 1$ , additional samples are added according to Section 2.4.2 as  $\lfloor 0.15n_k \rfloor$ , resulting in a progressive growth of the sample set:  $\{70, 80, 92, 105, 120, 138, \dots\}$ . 637 638 639 640 641

Classical fixed designs do not allow incremental adjustment based on model uncertainty. For comparison, fixed designs of 70, 150, 300, 500, and 700 points are evaluated, with 700 representing the maximum sample size for both adaptive and classical strategies. 642 643 644

## 2.5.3 Incremental Neural Network Training 645

Adaptive sampling is coupled with incremental surrogate training. Starting from the initial design, the model is retrained as new samples are added, reducing overall model uncertainty progressively. Incremental training is implemented using the *Keras* library (Chollet et al., 2015), which allows updating model weights with new samples while preserving previously learned information. 646 647 648 649 650

Cross-validation is applied to estimate uncertainty across the entire sample space. To avoid biasing uncertainty estimation toward newly added points, incremental retraining is reserved for the final model. This approach maintains both computational efficiency and accurate representation of global uncertainty. 651 652 653 654

Overall, this experimental design systematically investigates the influence of temporal instance selection, sample size, and adaptive incremental training on surrogate model performance, directly addressing this work’s hypotheses. 655 656 657

## 2.5.4 Carbon Footprint Analysis 658

The accelerating impacts of climate change and global environmental degradation have led to international commitments such as the Paris Climate Change Agreement (PCCA), through which almost all countries have agreed to reduce their carbon emissions (Q. Wang et al., 2024). In this broader context, the rapid expansion of AI has garnered attention due to its substantial energy demands. Despite the potential of AI technologies to optimise energy use and promote environmental sustainability, their development and deployment are themselves energy-intensive processes that generate substantial greenhouse gas emissions. 659 660 661 662 663 664 665

The amount of computational power used for AI increased by 300,000 times between 2012 and 2018 (Freitag et al., 2021). Consequently, researchers have emphasised the 666 667

significance of adopting a "Green AI" approach, which prioritises computational efficiency and sustainability, as a contrasting approach to the current prevailing "Red AI" approach, which prioritises model accuracy without considering environmental cost (Freitag et al., 2021). This has led to the integration of monitoring tools to quantify and mitigate the energy consumption and carbon footprint of AI workloads.

This study employs CodeCarbon (Courty et al., 2024), an open-source software, to estimate  $CO_2$  emissions and energy consumption generated by training tasks. CodeCarbon records energy consumption from CPUs, GPUs, and memory, and converts these data into carbon-equivalent values based on the carbon intensity of the geographical region. This tool serves to complement traditional performance indicators, such as the  $R^2$ , with quantitative metrics that reflect environmental costs.

### 3. Results and discussion

To evaluate and validate the hypotheses and proposed methodology, the results are analyzed along three main dimensions: (1) the environmental impact of each strategy, quantified through its carbon footprint at the same steps; (2) computational costs associated with simulation, sampling, and training; and (3) model performance metrics achieved with each approach. Finally, these dimensions are jointly assessed to highlight the overall efficiency and sustainability attainable under each scenario.

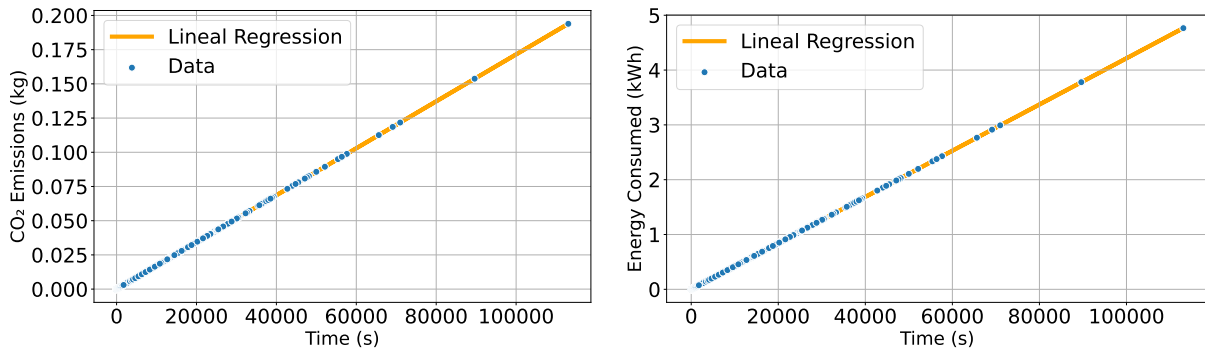
In the following sections, the results are presented using the following notation for each model: XGB refers to the XGBoost model trained with classical sampling, and XGBoost\_stochastic denotes the same model trained with adaptive sampling; CNN refers to the convolutional neural network trained with classical sampling, and CNN\_MC\_dropout indicates its adaptive sampling counterpart; finally, CNN\_ss denotes the self-supervised convolutional neural network trained with classical sampling, and CNN\_MC\_dropout\_ss refers to its adaptive sampling version.

#### 3.1 $CO_2$ emissions

The metrics recorded with CodeCarbon during the training sessions provided a detailed account of both  $CO_2$  emissions and energy consumption (kWh). The server was deployed in Sweden, and CodeCarbon automatically applied the Swedish energy data to calculate emissions and energy usage. Sweden was selected because it has one of the lowest emission intensities for electricity generation in Europe, as published in the report presented by the European Environment Agency (EEA) 'Greenhouse gas emission intensity of electricity generation in Europe', 2025.

Considering all the experiments carried out during this work, Figure 7 shows the relations between the  $CO_2$  emissions and energy consumption vs experiments computational temporal costs, subfigure 7a and 7b respectively.

The visible linear correlation is supported by a linear regression model, where the coefficient of determination ( $R^2$ ) approaches 1 (0.99999997 for both  $CO_2$  emissions and energy consumption). This indicates that time, according to CodeCarbon, is the primary factor influencing both emissions and energy use during the training processes. Consequently, the following sections will directly evaluate the environmental impact of the experiments in respect of time, as this is a reliable indicator of the overall impact.



(a)  $CO_2$  emissions (kg) over time (s)

$$\hat{y} = 0.00000172x + -0.00000013$$

(b) Energy consumed (kWh) over time (s)

$$\hat{y} = 0.00004215x + -0.00000309$$

Figure 7: CodeCarbon metrics with respect to duration

### 3.2 Computational cost

When assessing the computational cost required to fit a surrogate model, it is necessary to measure the execution time of each step in the process. Specifically, the fitting of a surrogate model involves three main stages: (1) data generation through simulations, (2) sample selection using a sampling method, and (3) model training.

The methodology proposed in this work focuses on the sampling strategies and the models themselves. Therefore, in order to enable a fair comparison across all experiments, the computational costs analyzed correspond to stages (1), (2) and (3).

Regarding data generation, in this case all simulations are performed with the same physical model. Consequently, the computational cost of generating simulated samples is constant, disregarding minor fluctuations due to background processes of the computing system.

However, the scope of the surrogate model strongly depends on both the quantity and the quality of the available data. For this reason, it is still essential to consider the number of samples, although this aspect will be analyzed in a later section, as the objective is to maximize model performance with the minimum amount of data. Importantly, in the context of more complex physical models, such as full *Phase field* simulations, the computational cost of data generation becomes a critical factor, where both the number of samples and the total simulation time play a decisive role.

The following subsections analyze the computational costs associated with each of the steps outlined above.

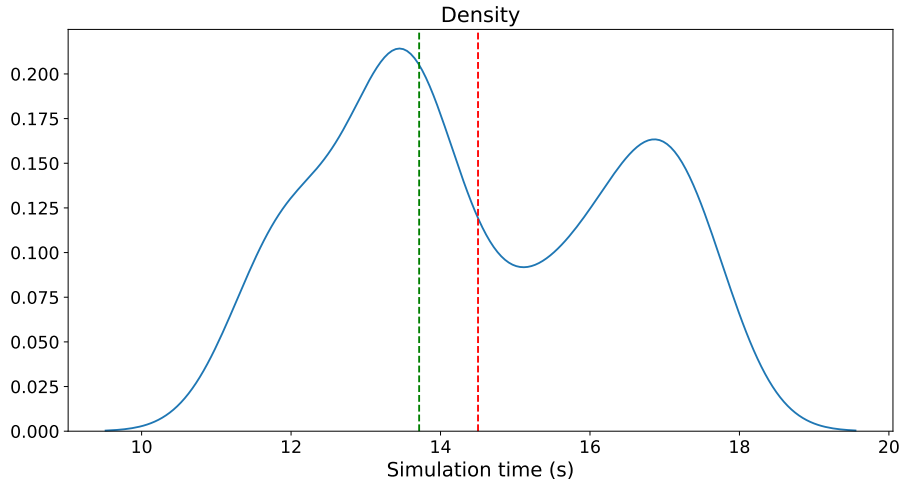


Figure 8: Density distribution of the time required to simulate a single sample by the phase field model.

### 3.2.1 Simulations temporal cost

731

To approximate the simulation time of the original physical model, the computational cost of all simulations was recorded. Figure 8 shows the density distribution of the simulation times, where the vertical lines indicate the mean (red) and the median (green), which are 14.5s and 13.7s, respectively.

735

### 3.2.2 Sampling temporal cost

736

As mentioned above, two sampling methods were considered: classical and adaptive. For the classical method, the computational cost corresponds to the time required to generate the samples for a given sample size, namely {70, 150, 300, 500, 700}.

739

In the case of adaptive sampling, the computational cost for a sample size  $n_k$  must also include the accumulated cost of all previous iterations, i.e.,  $n_0, \dots, n_{k-1}$ . This is because reaching  $n_k$  samples requires  $k$  iterations of the method. Thus, in addition to the initial classical sampling, the adaptive method is executed  $k$  times.

743

Figure 9 presents the results for the three experimental instances. Each plot shows the computational cost (time) for each model and sampling size. The same colors are used for each type of model, while lighter shades indicate the cost of the classical sampling methodology, in contrast with the adaptive method.

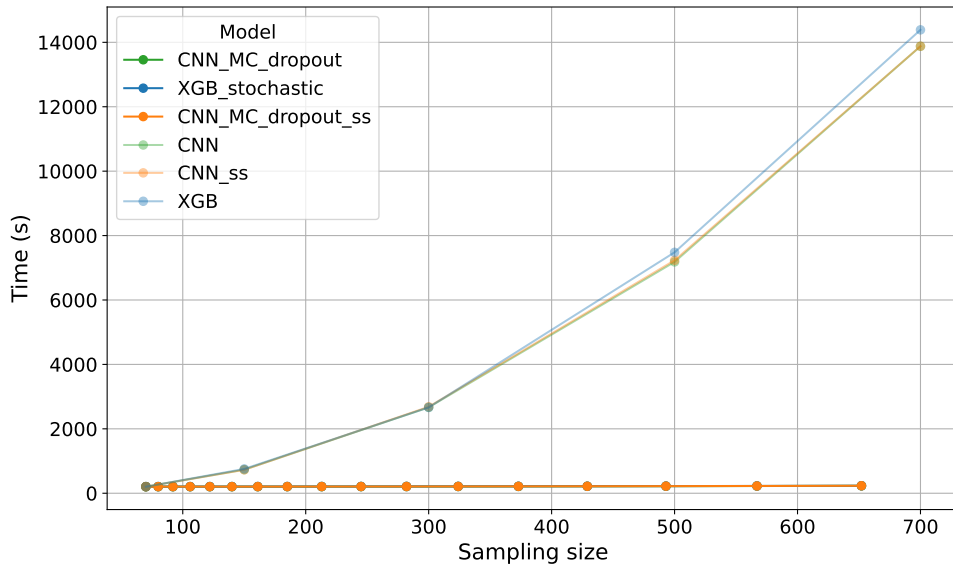
747

The number of training instances and the images used do not influence the sampling method, since the latter only selects which parameters of the physical model should be used to generate new samples in order to improve the surrogate model uncertainty. As shown in Figure 9, the cost of each method depends solely on the sample size, with no impact from the model itself. Moreover, the results clearly indicate that adaptive sampling entails significantly lower computational costs compared to classical sampling.

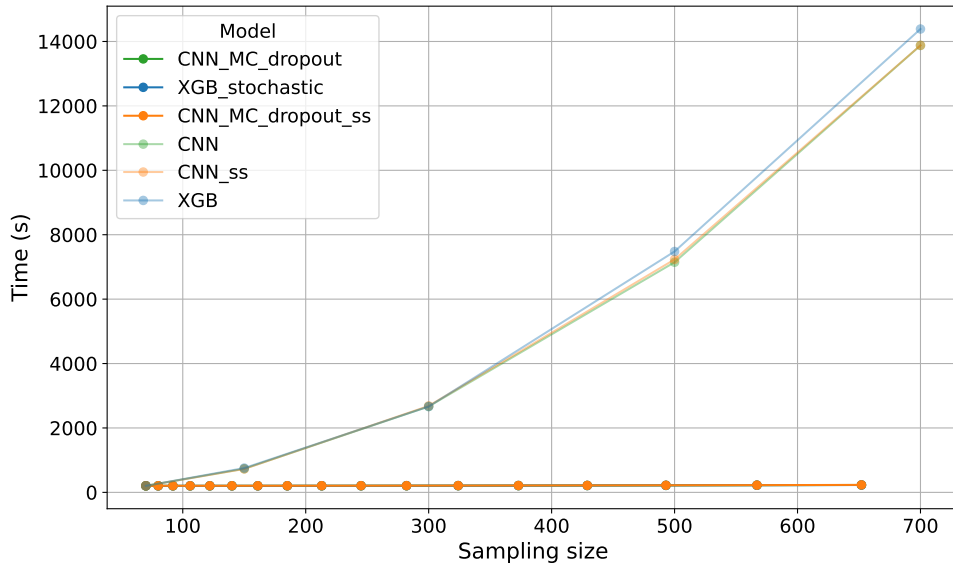
753

The difference between the two strategies is noteworthy. Adaptive sampling is iterative and accumulates cost over successive iterations. Nevertheless, this does not prevent it from

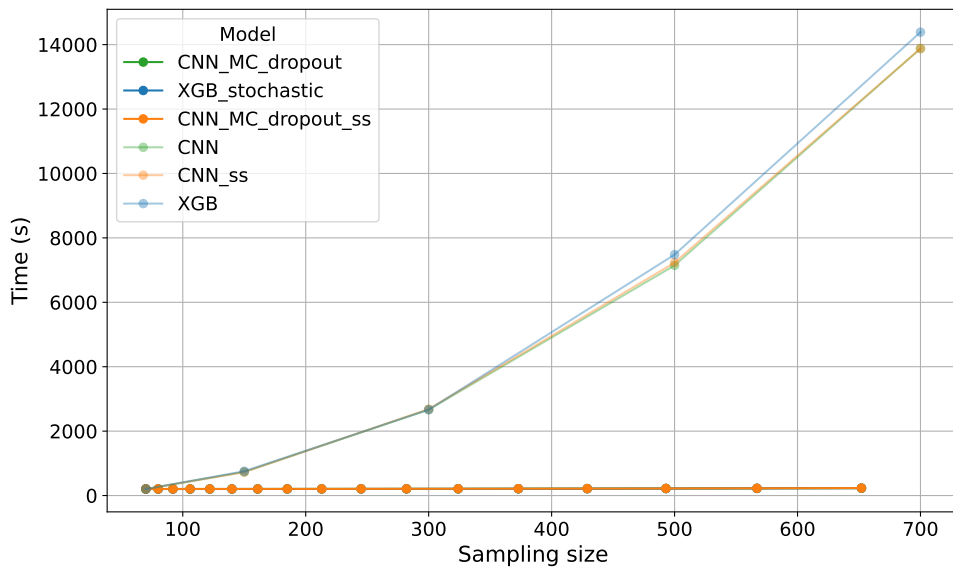
755



(a) Sampling cost for training instance ID1.



(b) Sampling cost for training instance ID2.



(c) Sampling cost for training instance ID3.

Figure 9: Computational cost of sampling for each group of training instances, across all models and both sampling methods.

being more efficient, since compared to classical sampling it achieves substantially lower computational times. This may be due to the fact that in each iteration only a small number of samples (15% of the previous iteration) are added, which can lead to greater efficiency compared to distance-based sampling strategies.

On the other hand, classical methods rely on a single initial exploration of the design space, which results in much higher computational costs. This problem becomes especially challenging in high-dimensional spaces, as the method aims to maximize distances between samples, a task that is computationally expensive. In other words, when using distance-based strategies with large sample sizes, the computational cost of classical sampling grows rapidly, and the method loses efficiency.

When comparing the emission values of  $CO_2$  and energy consumption for each sampling method and their corresponding sample sizes and models, we can extrapolate all the results and conclusions obtained for the computational cost in time, as shown in subsection 3.1 the corresponding  $R^2$  between the temporal cost and emissions and the temporal cost and energy consumption is practically 1 in both cases. Therefore, carbon emissions are very similar for the 3 models and time instance experiments for the case of the adaptive sampling, with the values showing negligible variation as the number of samples increases, getting all values within  $3.469 \cdot 10^{-4}kg$  and  $3.972 \cdot 10^{-4}kg$ , and similar happens for the energy consumption, getting values within  $8.501 \cdot 10^{-3}kWh$  and  $9.733 \cdot 10^{-3}kWh$ . In the case of the classical method, the values are also similar across all models and time-instance experiments; however, both carbon emissions and energy consumption increase considerably as the number of samples grows, reaching values between  $3.493 \cdot 10^{-4}kg$  and  $2.387 \cdot 10^{-2}kg$  for the  $CO_2$  emissions and values between  $8.561 \cdot 10^{-3}kWh$  and  $5.849 \cdot 10^{-1}kWh$  for the energy consumption.

The results clearly show this effect: classical sampling struggles to identify spatially scattered sets of distant samples, which has negative consequences for computational efficiency. By contrast, adaptive sampling, through its iterative construction of the design space and strategic selection of new samples, keeps computational costs under control.

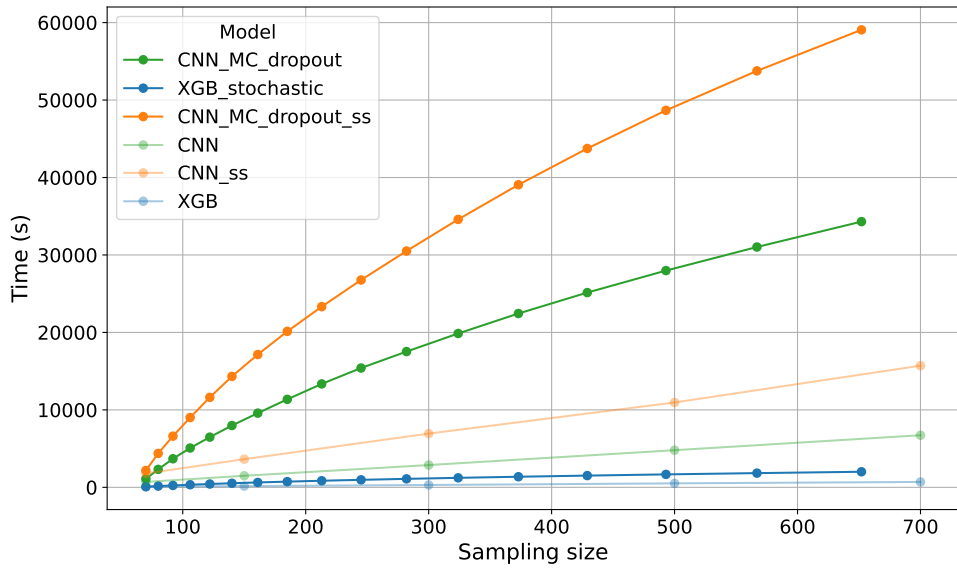
### 3.2.3 Training temporal cost

When training surrogate models with classical and adaptive sampling, it should be noted that in the former case, the model is trained only once, whereas in the latter, training is repeated for each newly added batch of samples.

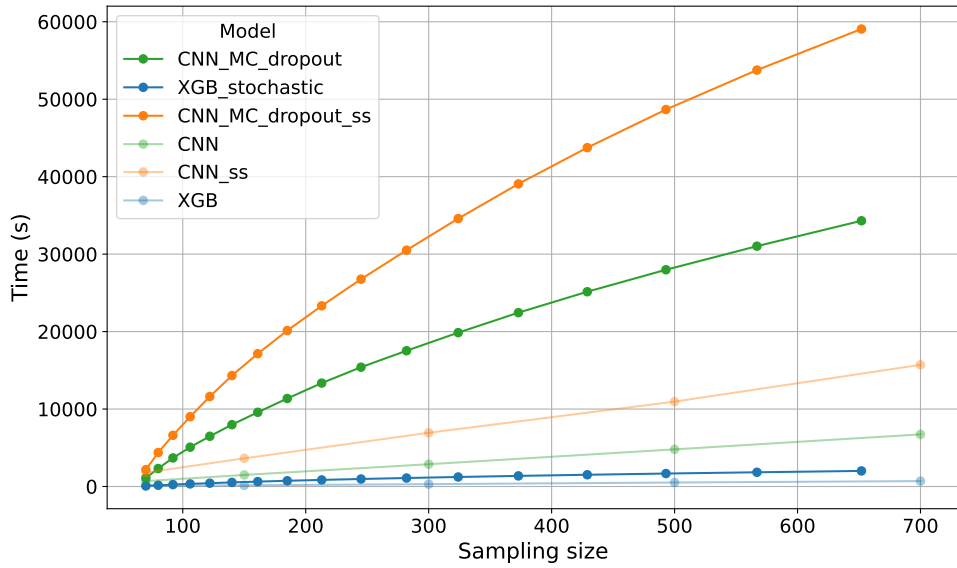
Therefore, for adaptive sampling, the actual time required to train the  $k$ -th surrogate model must consider the cumulative computational cost of all models trained from the initial sample set up to the  $k$ -th iteration.

The computational costs for all models, across different sample sizes and both sampling methods, are shown in Figure 10.

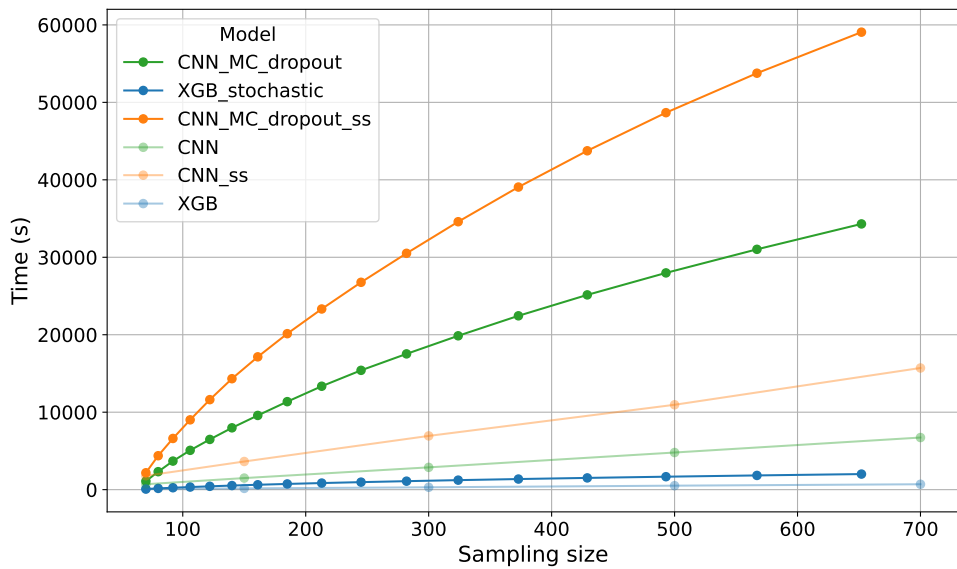
Comparing the results across the three training instance experiments, it is evident that the trends among models are consistent. It is also important to highlight that



(a) Training cost of surrogate models for training instance ID1.



(b) Training cost of surrogate models for training instance ID2.

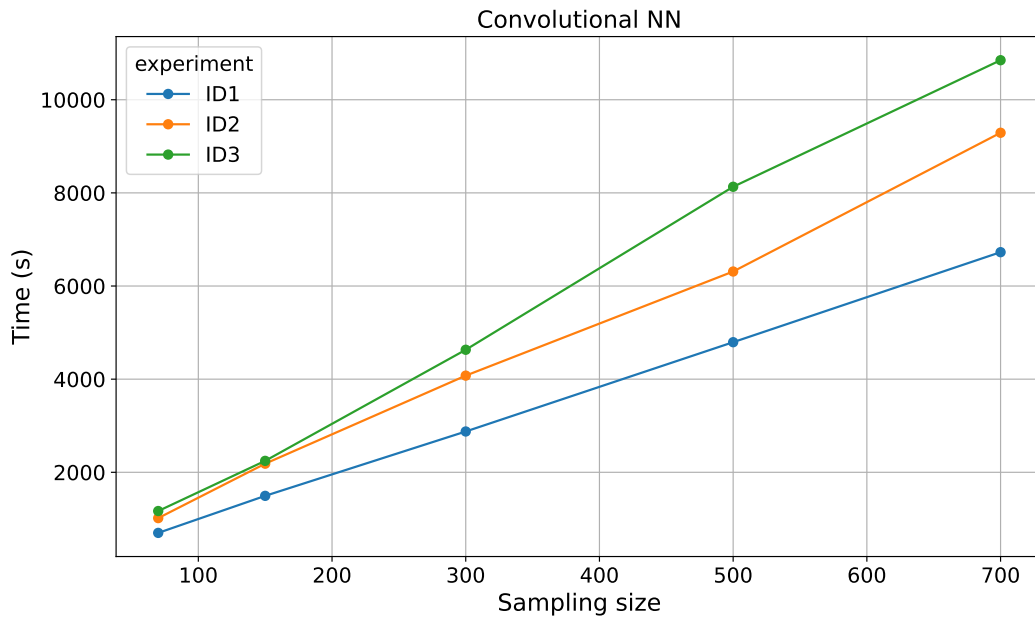


(c) Training cost of surrogate models for training instance ID3.

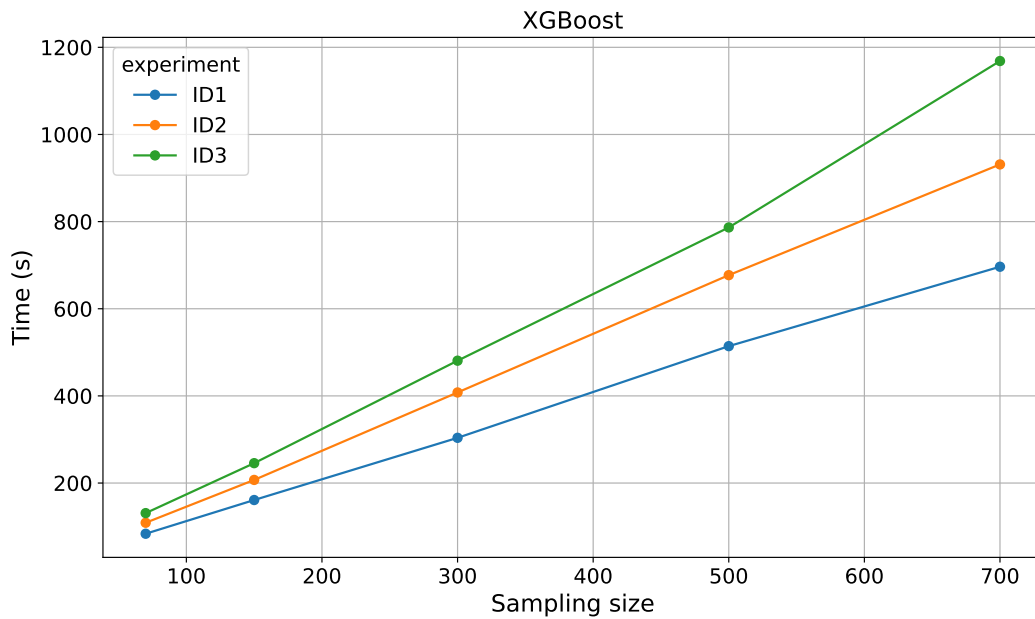
Figure 10: Computational cost of training surrogate models for each group of training instances, for both sampling methods.

the computational cost depends on the amount of data and the number of parameters to optimize. Although the trends remain similar across the three instance sets, an increase in the number of training instances directly translates into higher computational cost. This effect is particularly pronounced in neural networks. For example, training a convolutional neural network with classical sampling for *ID1* requires approximately 7000s, whereas for the same model, the cost rises to between 10000 and 11000s for *ID2* and *ID3*.

The variation of computational cost across the three training instance sets is illustrated in Figure 11 for convolutional neural networks and XGBoost. Similar trends are observed for the remaining models.



(a) Computational cost of convolutional neural network training.



(b) Computational cost of XGBoost training.

Figure 11: Training computational cost of surrogate models across different training instance sets.

Again, referring to Figure 10, it is clear that, in general, training with adaptive 804  
sampling incurs higher costs compared to classical sampling. As expected, cumulative 805  
training costs increase iteratively with each added batch of samples, whereas classical 806  
sampling trains only once. 807

However, in convolutional neural networks, the relationship between sample size and 808  
computational time is approximately linear for classical sampling, but not for adaptive 809  
sampling. Specifically, adaptive sampling exhibits a concave curve, with the derivative 810  
decreasing as more samples are added. This effect is attributed to incremental training: 811  
although cross-validation is required to estimate uncertainty, the model is ultimately 812  
retrained with all data incrementally, which reduces the effective training time for each 813  
batch of new samples. 814

In the case of the environmental cost associated with the training phase, as with the 815  
sampling cost, the results and conclusions are also directly extrapolable, because of the  $R^2$  816  
values obtained in subsection 3.1. More precisely, in these cases, both  $CO_2$  emissions and 817  
energy consumption rise as the number of instances in the temporal experiments increases. 818  
In addition, it can be observed that the results of the adaptive method are higher and 819  
similar across all models, whereas in the classical method the increase is barely noticeable 820  
in comparison. All this leads to carbon dioxide emissions values between  $1.888 \cdot 10^{-3}kg$  821  
and  $8.901 \cdot 10^{-2}$  in the case of adaptive sampling, and an energy consumption between 822  
 $4.626 \cdot 10^{-2}kWh$  and  $2.181kWh$  for the same sampling method. In the case of the classical 823  
sampling, the  $CO_2$  emissions are between  $1.202 \cdot 10^{-3}kg$  and  $1.866 \cdot 10^{-2}kg$ , and energy 824  
consumptions between  $2.945 \cdot 10^{-2}kWh$  and  $4.573 \cdot 10^{-1}kWh$ . 825

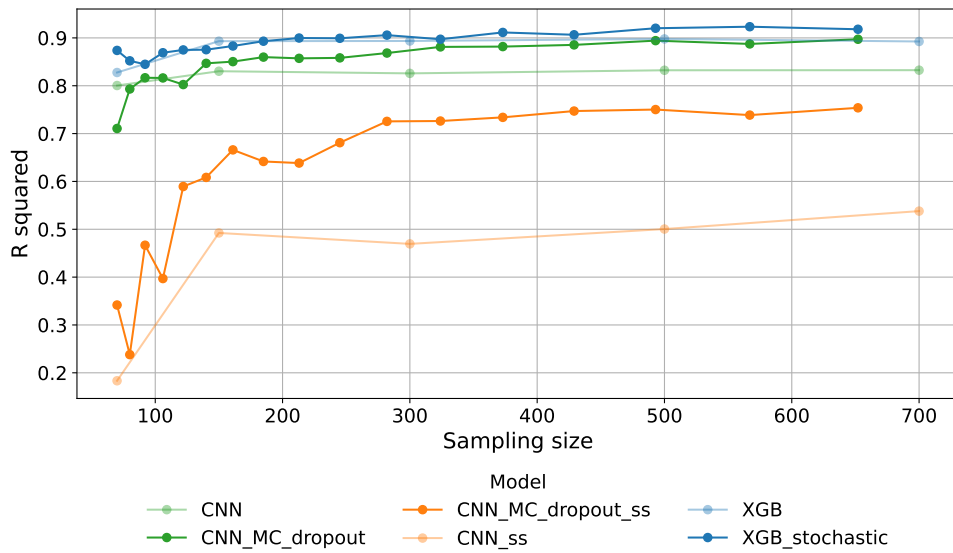
Finally, it is noteworthy that XGBoost exhibits particularly low computational costs 826  
compared to neural networks. Although adaptive sampling increases the training cost, 827  
it still improves performance relative to classical sampling in neural networks, achieving 828  
better accuracy for the same or lower computational expense. 829

### 3.3 Models performance 830

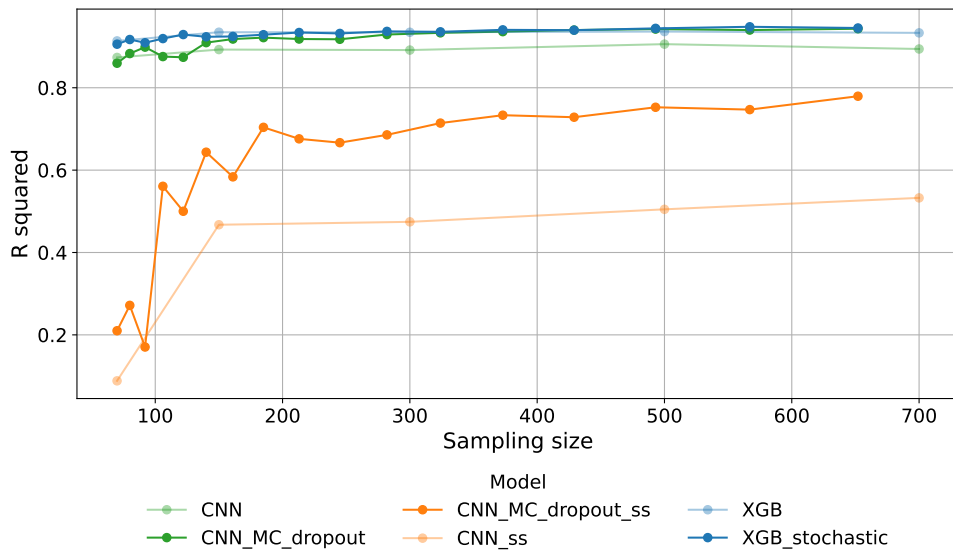
In this section, the performance metrics obtained for each model are compared. Specific- 831  
ally, the coefficient of determination ( $R^2$ ) was used to evaluate the fitting accuracy of the 832  
surrogate models. 833

The same plots used for comparing computational costs across models, training in- 834  
stance sets, and sampling methods are employed here. These results are shown in Figure 835  
12. 836

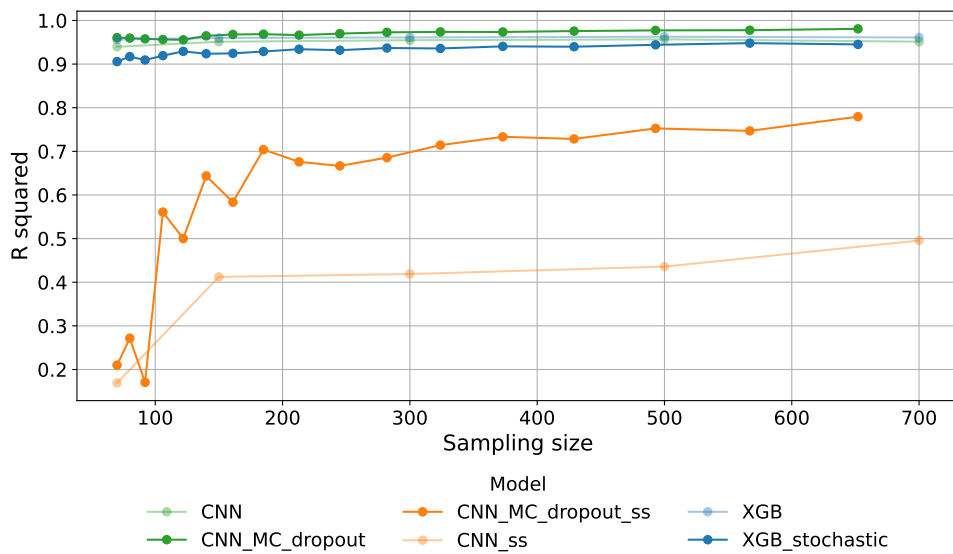
As observed in Figure 12, self-attentive convolutional neural networks do not achieve 837  
high performance, with  $R^2$  values remaining below 0.80 regardless of the sampling method 838  
or training instance set. However, adaptive sampling clearly improves performance com- 839  
pared to classical sampling. Specifically, no classical sampling experiment achieves  $R^2 >$  840  
0.50, while adaptive sampling yields values between 0.70 and 0.80 across the three training 841  
instance sets. 842



(a) Model performance metrics for training instance set ID1.



(b) Model performance metrics for training instance set ID2.



(c) Model performance metrics for training instance set ID3.

Figure 12: Fitting metrics obtained for each model across training instance sets and both sampling methods.

For convolutional neural networks, adaptive sampling consistently outperforms the self-attentive variant across all cases. Moreover, for all three training instance sets, adaptive sampling enhances the results obtained with classical sampling. The difference in  $R^2$  between the two methods decreases as the last training instance increases. Beyond reducing the difference, both models achieve higher performance metrics as the number of training instances grows. Notably, the best performance is obtained for *ID3*, while results in other experiments remain very close to the highest values.

In the case of XGBoost, excellent results are obtained across all three training instance sets. Specifically, the best outcomes occur for *ID1* and *ID2*, and for *ID3*, XGBoost performance closely approaches that of convolutional neural networks. Regarding the sampling methods, adaptive sampling improves results for *ID1* relative to classical sampling. For *ID2*, both methods yield very similar performance, and for *ID3*, classical sampling slightly outperforms adaptive sampling.

Finally, it is important to note that both convolutional neural networks and XGBoost achieve satisfactory initial performance, with  $R^2 > 0.7$  in all cases. As the sample size increases, fitting metrics improve gradually, approaching nearly perfect regression in some instances. However, the rate of improvement is relatively slow.

### 3.4 Discussion

Following the hypotheses and objectives outlined earlier, the following key points should be considered when selecting an appropriate surrogate model:

- Minimize the number of training instances whenever possible.
- Ensure that the last training instance used is sufficiently far from the final prediction instance.
- Achieve high fitting metrics with the smallest possible number of samples.
- Select a model that balances training cost and fitting performance.

As observed in previous results, increasing the number of training instances leads to higher training costs, particularly for neural networks.

Regarding the last training instance used, this choice carries significant weight. Instances closer to the prediction scenario tend to yield better fitting metrics. However, when deploying the surrogate model, greater dependency on the physical model may arise, potentially reducing the overall efficiency of the methodology. For example, in the case of *ID1*, an efficiently trained surrogate can reduce up to 50% of the original model's computational time for predictions. For *ID2*, this saving reaches up to 37.5%, and for *ID3*, only up to 12.5%.

The number of samples used for training is critical in scenarios where the physical model is computationally demanding. For instance, if one model requires 300 samples

to reach  $R^2 = 0.90$  and another only 150, the sampling cost can be reduced by 50%. 879  
When simulations require hours or days, achieving high accuracy with fewer samples is 880  
particularly important. 881

Finally, the balance between training cost and model accuracy must be maintained. 882  
Even if all previous conditions are satisfied, the training process must remain efficient; 883  
otherwise, the surrogate model will not offer meaningful computational savings relative 884  
to the original model. 885

Figure 13 illustrates the balance between the number of training instances, the last 886  
training instance, and the trade-off between fitting accuracy and computational cost for 887  
150, 500, and 700 samples. For adaptive sampling, results closest to these sample sizes are 888  
shown. Total computational cost includes sampling, simulation, and training; simulation 889  
cost is effectively constant for the same sample size across models. Thus, the cost reflects 890  
the trade-off between sampling and training. 891

Models that achieve a good balance between accuracy and computational cost include 892  
XGBoost with either classical or adaptive sampling, and convolutional neural networks 893  
with classical sampling. For convolutional networks with adaptive sampling, computa- 894  
tional cost increases significantly with sample size, but better results are obtained with 895  
fewer samples compared to classical sampling, maintaining the trade-off. 896

Regarding training instances, *ID3* experiments for XGBoost are unnecessary, as res- 897  
ults are very similar to *ID2*, while prediction savings are much larger. Between *ID1* 898  
and *ID2*, the choice should depend on simulation cost. For high-cost simulations, the 899  
accuracy offered by *ID1* may be sufficient considering prediction savings; if higher fitting 900  
is prioritized, *ID2* is preferable. 901

For convolutional networks, adaptive sampling increases computational cost, but small 902  
sample sizes (*ID1* and *ID2*) achieve good results, especially when considering the predic- 903  
tion cost of *ID3*. Specifically, with 150 samples and adaptive sampling for *ID2*, compu- 904  
tational cost and fitting metrics are much better than those obtained with 300 samples 905  
using classical sampling, as shown in Figures 13a and 13b. 906

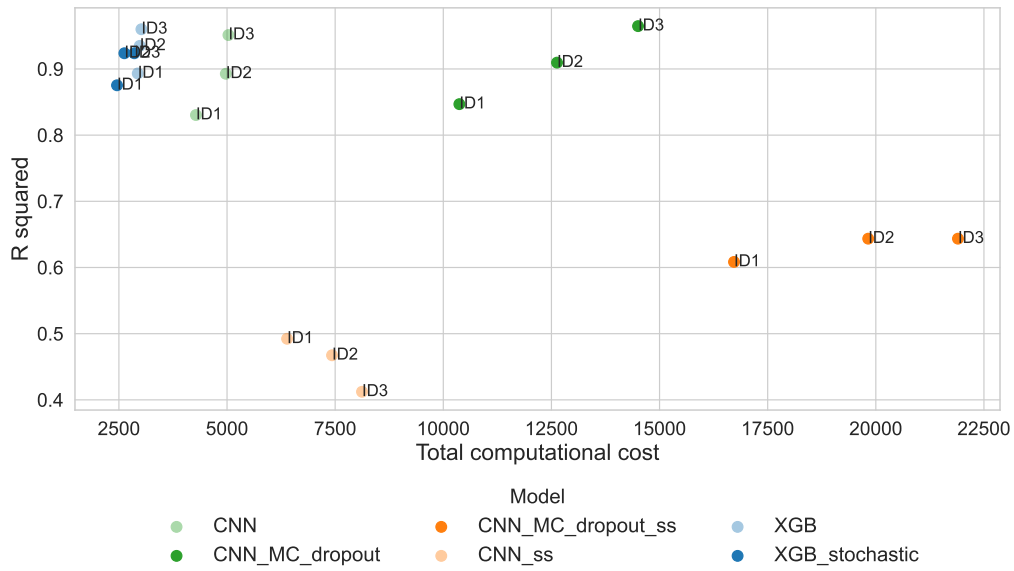
Self-attentive convolutional networks are generally not suitable as surrogate models, 907  
as the trade-off between computational cost and fitting accuracy is poor in all cases. 908

A main objective is to train a surrogate model that achieves high fitting metrics with 909  
minimal sample size. Following literature findings, this work hypothesizes that adaptive 910  
sampling allows training a more accurate model with fewer samples. 911

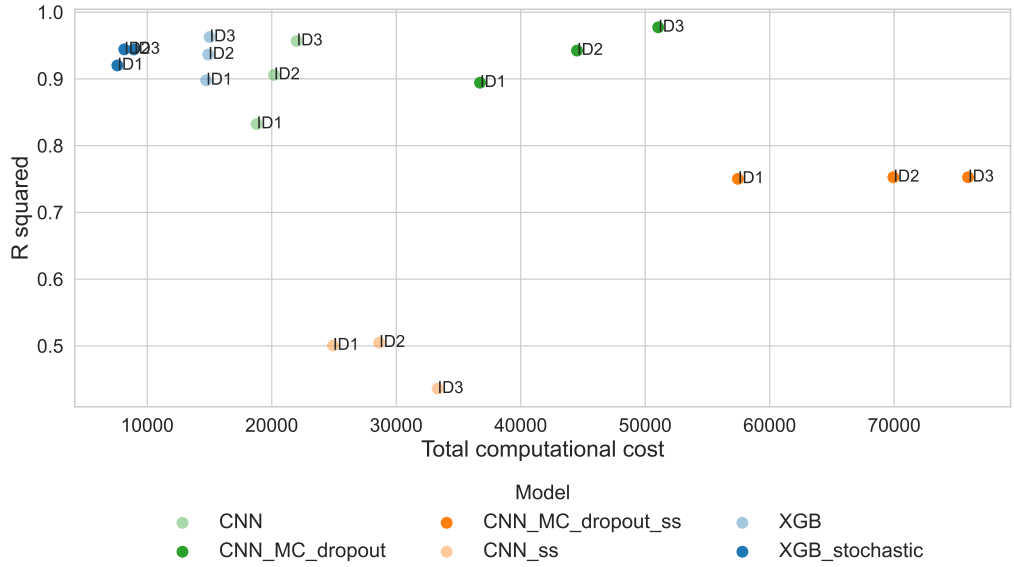
To test this hypothesis, a comparison was performed between the number of samples 912  
and computational cost required to achieve the maximum  $R^2$  with classical sampling 913  
versus adaptive sampling. 914

The results are summarized in Table 2 and visually in Figure 14. 915

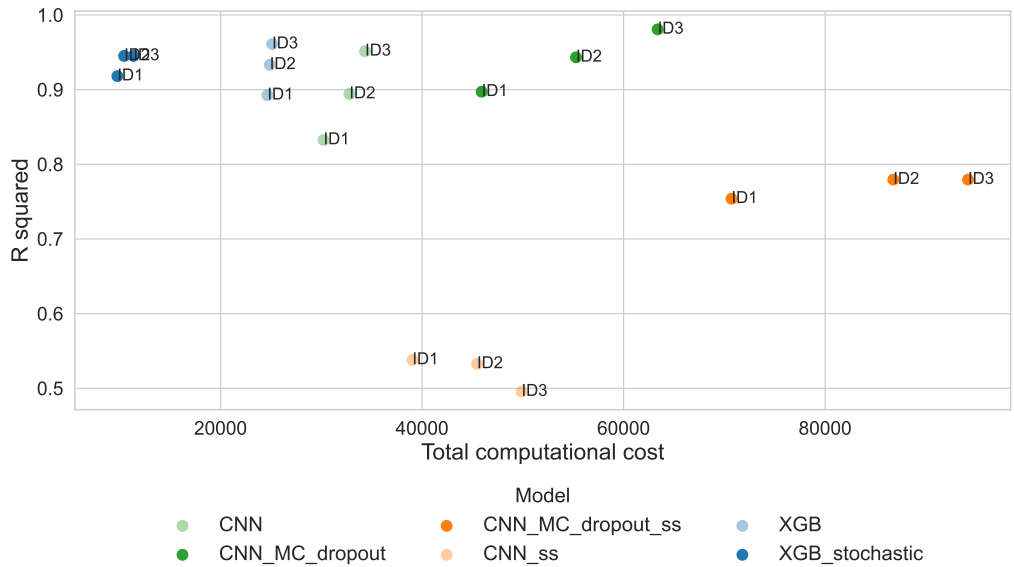
As shown in Table 2 and Figure 14, except for *ID3* experiments with XGBoost, ad- 916  
aptive sampling requires fewer samples to reach the maximum classical  $R^2$ , substantially 917  
reducing simulation time. For example, in XGBoost with *ID1*, adaptive sampling achieves 918



(a) Total computational cost and  $R^2$  for 150 samples

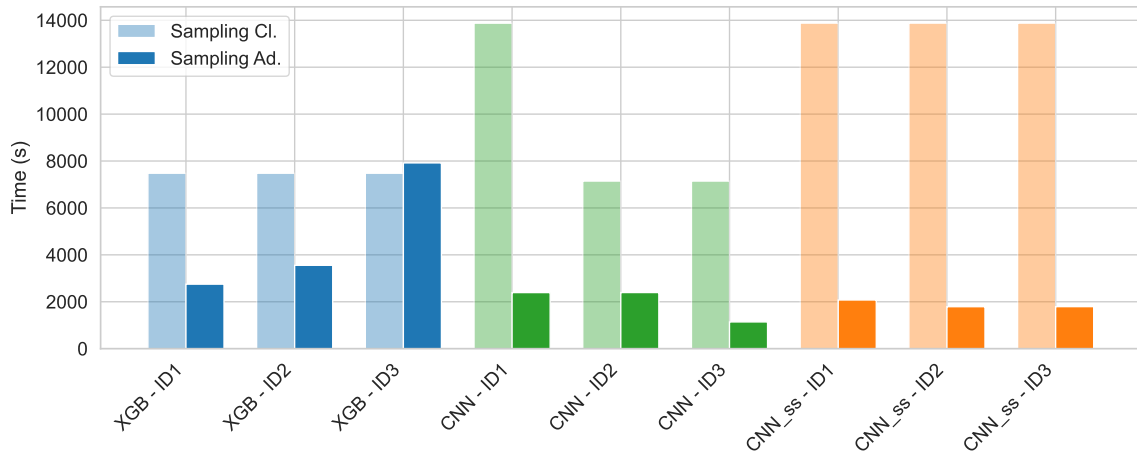


(b) Total computational cost and  $R^2$  for 500 samples

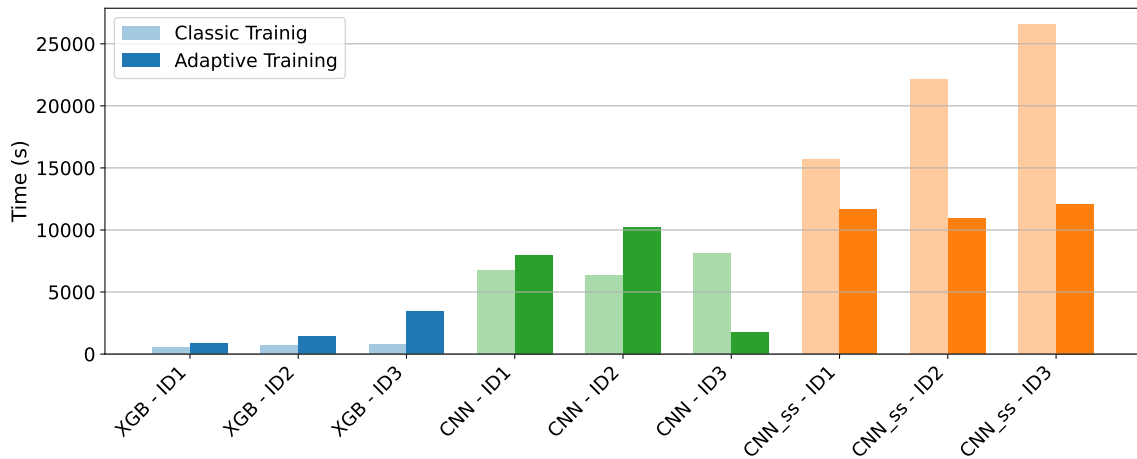


(c) Total computational cost and  $R^2$  for 700 samples

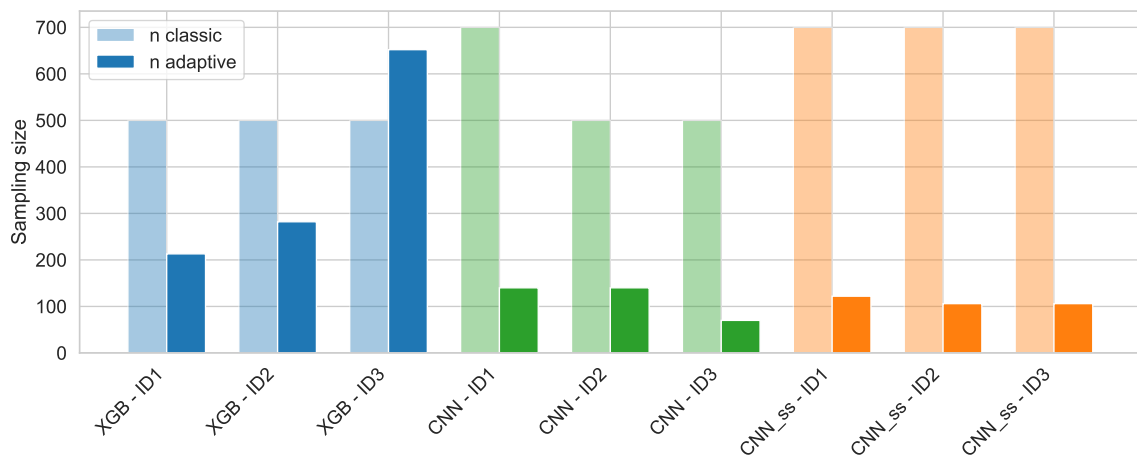
Figure 13: Trade-off between total computational cost and  $R^2$  across training instance sets and models for different sample sizes.



(a) Sampling cost to reach maximum classical  $R^2$



(b) Training cost to reach maximum classical  $R^2$



(c) Comparison of sample numbers to reach maximum classical  $R^2$

Figure 14: Computational costs in sampling and training, and number of samples, required by each method to reach the maximum  $R^2$  achieved with classical sampling.

Model	ID	Max $R^2$ (classical)	n (classical)	Train t (classical)	Sample t (classical)	n (adaptive)	Train t (adaptive)	Sample t (adaptive)
XGB	ID1	0.899	500	514.18	7479.67	213	850.77	2750.05
XGB	ID2	0.936	500	677.12	7479.67	282	1426.40	3553.86
XGB	ID3	0.963	500	786.60	7479.67	652	3434.85	7919.31
CNN	ID1	0.833	700	6726.77	13877.10	140	7981.12	2390.51
CNN	ID2	0.906	500	6311.46	7145.37	140	10237.30	2392.34
CNN	ID3	0.957	500	8131.22	7145.37	70	1727.71	1139.70
CNN_ag	ID1	0.538	700	15707	13879.80	122	11618.60	2075.11
CNN_ag	ID2	0.533	700	22119.40	13879.80	106	10954.80	1788.75
CNN_ag	ID3	0.496	700	26538.50	13879.80	106	12092.20	1791.29

Table 2: Computational cost and number of samples required by each method to reach the maximum classical  $R^2$ .

a 57.4% saving in simulation cost. On average, across all experiments, 65.7% of simulation time could be saved with adaptive sampling.

As previously noted, adaptive sampling is computationally more efficient than classical sampling when considering the time to select samples. Combined with achieving the same accuracy with fewer samples (Figure 14b), adaptive sampling provides significantly better computational efficiency in most cases.

Finally, although the cumulative computational cost of models trained with adaptive sampling is higher than that of classical sampling, reaching the same fitting metrics with fewer samples reduces the overall cost, as shown in Figure 14a. Except for self-attentive convolutional networks, training costs are higher but more balanced across the remaining models.

## 4. Conclusions

The main goal of this work has been to identify an appropriate surrogate modelling strategy for the spatio-temporal nature of dendritic solidification simulations, with the aim of reducing the computational cost of the original phase field model. To this end, the study has examined how different modelling choices, the selection of temporal training instances, the sampling methodology, and the model, have influenced the number of required samples, the computational cost and the final predictive performance of the surrogate. Since each sample corresponds to an expensive phase field simulation, minimizing the number of samples has been essential for reducing total computational effort. The evaluation has been conducted through quantitative metrics capturing surrogate accuracy ( $R^2$ ), computational time, training and sampling costs, and their associated energy consumption and  $CO_2$  emissions. Training time exhibited an almost perfectly linear correlation with environmental indicators, thus, it has served as a consistent basis for assessing the trade-off between sustainability, computational efficiency, and surrogate-model performance.

The comparison between the classical and adaptive sampling methods proposed revealed clear differences. Classical sampling, based on an Optimal Latin Hypercube Sampling conducted by the PSO algorithm, struggles to remain computationally efficient as the number of samples increases, since the optimization is distance-based and its cost grows accordingly, leading to higher sampling costs. For the proposed adaptive sampling

method, the cost associated with identifying new samples is lighter than in the classical 950  
approach, because new points are added iteratively and the search process is designed 951  
to minimise its computational impact. In addition, the method progressively refines the 952  
design space and incorporates uncertainty—estimated through cross-validation—to guide 953  
the selection of new samples. While this strategy increases training time, since the model 954  
must be retrained at every iteration, it generally reduces the total number of samples 955  
required to reach a given accuracy. As a result, adaptive sampling achieves better sample 956  
efficiency and reduces the simulation cost in most experiments. 957

Regarding the comparison between the convolutional models—which automatically ex- 958  
tract spatial features—and the XGB model—which relies on a domain-knowledge-based 959  
feature transformation—the training cost of the CNNs is consistently higher, as they must 960  
optimise a significantly larger number of parameters. Furthermore, as mentioned previ- 961  
ously, the total training cost in the adaptive approach is also higher, since it accumulates 962  
the training effort required at each iteration. This cost is further increased by the need to 963  
estimate model uncertainty across the entire design space: in the current implementation, 964  
this is achieved through cross-validation, which adds an additional computational burden 965  
to every adaptive iteration. 966

When comparing the different sets of temporal instances, it can be observed that—except 967  
for the self-supervised models—better predictive metrics are obtained when the final time 968  
 $t_f$  is closer to the target solidification state. This improvement, however, comes at the 969  
expense of a slight increase in computational cost. Considering these results together with 970  
the simulation time required when using the surrogate for prediction, we conclude that 971  
the best balance between performance and computational efficiency is achieved with the 972  
*ID1* and *ID2* configurations. 973

Finally, in terms of the trade-off between training cost and predictive performance, the 974  
XGB model achieves the best overall balance, largely due to the efficiency of the domain- 975  
knowledge-based feature extraction employed. However, although adaptive sampling re- 976  
duces the number of required samples for both modelling approaches, the reduction is 977  
substantially more pronounced for the CNN. This is relevant because, unlike XGB—which 978  
benefits heavily from the handcrafted feature transformation and thus depends on prior 979  
knowledge of the problem—the CNN learns spatial representations directly from the data. 980  
Consequently, when combined with the adaptive sampling strategy, the CNN can achieve 981  
competitive performance with significantly fewer samples. This not only enhances its po- 982  
tential for generalisation in scenarios where domain knowledge is limited, but also enables 983  
a notable reduction in the number of phase field simulations required, and therefore in 984  
the computational cost associated with generating the training data. 985

Future work would explore several directions aimed at further improving the modelling 986  
and training efficiency of the proposed framework. First, incorporating architectures cap- 987  
able of capturing both spatial and temporal correlations, such as recurrent-convolutional 988  
hybrids or attention-based spatio-temporal models, would allow a more precise represent- 989

ation of the underlying space-time dynamics without discarding temporal dependencies 990  
between frames. Second, strategies that reduce the reliance on the original phase field 991  
model during inference would be investigated, for example through autoregressive sur- 992  
rogate formulations that predict successive states from previous surrogate outputs while 993  
controlling the accumulated error. Third, the methodology should be evaluated on more 994  
computationally demanding phase field formulations, including higher-resolution 2D and 995  
fully 3D cases. Fourth, developing more computationally efficient uncertainty-estimation 996  
techniques would further reduce the overhead of the adaptive sampling procedure. Finally, 997  
physics-informed neural network (PiNN) approaches could be considered as a means to 998  
embed physical constraints directly into the surrogate, potentially improving generalisa- 999  
tion and reducing the amount of training data required. 1000

## Data Availability 1001

Data is generated using the phase-field model described in Biner, 2017. 1002

## Code Availability 1003

The code used to generate the results in this study will be made publicly available in 1004  
the future. In the meantime, the code may be shared upon reasonable request to the 1005  
corresponding author. 1006

## Acknowledgments 1007

This work has been supported by an Elkartek project funded by the Basque Government 1008  
for basic research. 1009

## Author Contributions 1010

Eider Garate-Perez: Conceptualization, Methodology, Software/Coding, Validation, Formal 1011  
Analysis, Investigation, Data Curation, Writing – Original Draft, Writing – Review & 1012  
Editing, Visualization. Kerman López de Calle-Etxabe: Conceptualization, Methodo- 1013  
logy, Resources, Writing – Review & Editing, Supervision, Funding Acquisition. Oihana 1014  
Garcia: Software/Coding, Validation, Formal Analysis, Investigation, Writing – Original 1015  
Draft, Writing – Review & Editing, Visualization. Borja Calvo: Conceptualization, Meth- 1016  
odology, Writing – Review & Editing, Supervision. Meritxell Gómez-Omella: Conceptu- 1017  
alization, Methodology, Software/Coding, Writing – Review & Editing. Jon Lambarri: 1018  
Software/Coding, Writing – Review & Editing. 1019

<b>Competing Interests</b>	1020
The authors declare no competing interests.	1021
<b>Preprint notice</b>	1022
This manuscript is a preprint and has not yet been peer-reviewed.	1023
<b>References</b>	1024
Afzal, A., Kim, K.-Y., & Seo, J.-w. (2017). Effects of Latin hypercube sampling on surrogate modeling and optimization. <i>International Journal of Fluid Machinery and Systems</i> , 10(3), 240–253. <a href="https://doi.org/10.5293/IJFMS.2017.10.3.240">https://doi.org/10.5293/IJFMS.2017.10.3.240</a>	1025 1026 1027
Ahmad, O., Kumar, N., Mukherjee, R., & Bhowmick, S. (2023). Accelerating microstructure modeling via machine learning: A method combining Autoencoder and ConvLSTM. <i>Physical Review Materials</i> , 7(8), 083802. <a href="https://doi.org/10.1103/PhysRevMaterials.7.083802">https://doi.org/10.1103/PhysRevMaterials.7.083802</a>	1028 1029 1030 1031
Alizadeh, R., Allen, J. K., & Mistree, F. (2020). Managing computational complexity using surrogate models: A critical review. <i>Research in Engineering Design</i> , 31(3), 275–298. <a href="https://doi.org/10.1007/s00163-020-00336-7">https://doi.org/10.1007/s00163-020-00336-7</a>	1032 1033 1034
Azarhoosh, Z., & Ilchi Ghazaan, M. (2025). A Review of Recent Advances in Surrogate Models for Uncertainty Quantification of High-Dimensional Engineering Applications. <i>Computer Methods in Applied Mechanics and Engineering</i> , 433, 117508. <a href="https://doi.org/10.1016/j.cma.2024.117508">https://doi.org/10.1016/j.cma.2024.117508</a>	1035 1036 1037 1038
Aziz, M., & Tayarani- N., M. H. (2014). An adaptive memetic Particle Swarm Optimization algorithm for finding large-scale Latin hypercube designs. <i>Engineering Applications of Artificial Intelligence</i> , 36, 222–237. <a href="https://doi.org/10.1016/j.engappai.2014.07.021">https://doi.org/10.1016/j.engappai.2014.07.021</a>	1039 1040 1041 1042
Bhagat, K., & Rudraraju, S. (2023). Modeling of dendritic solidification and numerical analysis of the phase-field approach to model complex morphologies in alloys. <i>Engineering with Computers</i> , 39(4), 2345–2363. <a href="https://doi.org/10.1007/s00366-022-01767-7">https://doi.org/10.1007/s00366-022-01767-7</a>	1043 1044 1045 1046
Biner, S. B. (2017). <i>Programming Phase-Field Modeling</i> . Springer International Publishing. <a href="https://doi.org/10.1007/978-3-319-41196-5">https://doi.org/10.1007/978-3-319-41196-5</a>	1047 1048
Borisut, P., & Nuchitprasittichai, A. (2023). Adaptive Latin Hypercube Sampling for a Surrogate-Based Optimization with Artificial Neural Network. <i>Processes</i> , 11(11), 3232. <a href="https://doi.org/10.3390/pr11113232">https://doi.org/10.3390/pr11113232</a>	1049 1050 1051
Brophy, J., & Lowd, D. (2022). Instance-Based Uncertainty Estimation for Gradient-Boosted Regression Trees [Version Number: 2]. <a href="https://doi.org/10.48550/ARXIV.2205.11412">https://doi.org/10.48550/ARXIV.2205.11412</a>	1052 1053 1054

- Chen, X., Ding, M., Wang, X., Xin, Y., Mo, S., Wang, Y., Han, S., Luo, P., Zeng, G., & Wang, J. (2024). Context Autoencoder for Self-supervised Representation Learning. *International Journal of Computer Vision*, 132(1), 208–223. <https://doi.org/10.1007/s11263-023-01852-4>
- Choi, J. Y., Xue, T., Liao, S., & Cao, J. (2024). Accelerating phase-field simulation of three-dimensional microstructure evolution in laser powder bed fusion with composable machine learning predictions. *Additive Manufacturing*, 79, 103938. <https://doi.org/10.1016/j.addma.2023.103938>
- Chollet, F., et al. (2015). Keras [Accessed: 2025-07-01].
- Courty, B., Schmidt, V., Luccioni, S., & and, G.-K. (2024, May). *Mlco2/codecarbon: V2.4.1* (Version v2.4.1). Zenodo. <https://doi.org/10.5281/zenodo.11171501>
- Dantzig, J. A., & Rappaz, M. (2009). *Solidification*. EPFL press CRC press.
- Di Fiore, F., Nardelli, M., & Mainini, L. (2024). Active Learning and Bayesian Optimization: A Unified Perspective to Learn with a Goal. *Archives of Computational Methods in Engineering*, 31(5), 2985–3013. <https://doi.org/10.1007/s11831-024-10064-z>
- Dobravec, T., Mavrič, B., Zahoor, R., & Šarler, B. (2023). A coupled domain–boundary type meshless method for phase-field modelling of dendritic solidification with the fluid flow. *International Journal of Numerical Methods for Heat & Fluid Flow*, 33(8), 2963–2981. <https://doi.org/10.1108/HFF-03-2023-0131>
- Duquesnoy, M., Liu, C., Dominguez, D. Z., Kumar, V., Ayerbe, E., & Franco, A. A. (2023). Machine learning-assisted multi-objective optimization of battery manufacturing from synthetic data generated by physics-based simulations. *Energy Storage Materials*, 56, 50–61. <https://doi.org/10.1016/j.ensm.2022.12.040>
- Escobar-Cuevas, H., Cuevas, E., Avila, K., & Avalos, O. (2024). An advanced initialization technique for metaheuristic optimization: A fusion of Latin hypercube sampling and evolutionary behaviors. *Computational and Applied Mathematics*, 43(4), 234. <https://doi.org/10.1007/s40314-024-02744-0>
- Fakour, F., Mosleh, A., & Ramezani, R. (2024). A Structured Review of Literature on Uncertainty in Machine Learning & Deep Learning [Version Number: 1]. <https://doi.org/10.48550/ARXIV.2406.00332>
- Fassi, H. F., & Aniyu, H. (2023). Towards an Optimal Motor Mounting Bracket Using Topology Optimization Combined with Sustainability and Manufacturing Cost Analysis. *Management and Production Engineering Review*. <https://doi.org/10.24425/mper.2023.147208>
- Forrester, A. I., & Keane, A. J. (2009). Recent advances in surrogate-based optimization. *Progress in Aerospace Sciences*, 45(1-3), 50–79. <https://doi.org/10.1016/j.paerosci.2008.11.001>

- Freitag, C., Berners-Lee, M., Widdicks, K., Knowles, B., Blair, G. S., & Friday, A. (2021). The real climate and transformative impact of ict: A critique of estimates, trends, and regulations. *Patterns*, 2(9).
- Fuhg, J. N. (2019). Adaptive surrogate models for parametric studies [Version Number: 1]. <https://doi.org/10.48550/ARXIV.1905.05345>
- Fuhg, J. N., Fau, A., & Nackenhorst, U. (2021). State-of-the-Art and Comparative Review of Adaptive Sampling Methods for Kriging. *Archives of Computational Methods in Engineering*, 28(4), 2689–2747. <https://doi.org/10.1007/s11831-020-09474-6>
- Gal, Y., & Ghahramani, Z. (2015). Dropout as a Bayesian Approximation: Representing Model Uncertainty in Deep Learning [Version Number: 6]. <https://doi.org/10.48550/ARXIV.1506.02142>
- Goswami, S., Anitescu, C., Chakraborty, S., & Rabczuk, T. (2020). Transfer learning enhanced physics informed neural network for phase-field modeling of fracture. *Theoretical and Applied Fracture Mechanics*, 106, 102447. <https://doi.org/10.1016/j.tafmec.2019.102447>
- Greenhouse gas emission intensity of electricity generation in europe.* (2025, June 27). European Environment Agency. Retrieved October 14, 2025, from <https://www.eea.europa.eu/en/analysis/indicators/greenhouse-gas-emission-intensity-of-1>
- Heid, E., McGill, C. J., Vermeire, F. H., & Green, W. H. (2023). Characterizing Uncertainty in Machine Learning for Chemistry. *Journal of Chemical Information and Modeling*, 63(13), 4012–4029. <https://doi.org/10.1021/acs.jcim.3c00373>
- Herman, E., Stewart, J. A., & Dingreville, R. (2020). A data-driven surrogate model to rapidly predict microstructure morphology during physical vapor deposition. *Applied Mathematical Modelling*, 88, 589–603. <https://doi.org/10.1016/j.apm.2020.06.046>
- Herten, J. V. D., Steenkiste, T. V., Couckuyt, I., & Dhaene, T. (2017, June). Surrogate Modelling with Sequential Design for Expensive Simulation Applications. In D. Cvetkovic (Ed.), *Computer Simulation*. InTech. <https://doi.org/10.5772/67739>
- Hoffmann, L., Fortmeier, I., & Elster, C. (2021). Uncertainty quantification by ensemble learning for computational optical form measurements. *Machine Learning: Science and Technology*, 2(3), 035030. <https://doi.org/10.1088/2632-2153/ac0495>
- Hüllermeier, E., & Waegeman, W. (2021). Aleatoric and epistemic uncertainty in machine learning: An introduction to concepts and methods. *Machine Learning*, 110(3), 457–506. <https://doi.org/10.1007/s10994-021-05946-3>
- Jarfors, A. E. W., Bogdanoff, T., & Lattanzi, L. (2024). Functionally integrated castings (Giga-castings) for body in white applications: Consequences for materials use and mix in automotive manufacturing. *Matériaux & Techniques*, 112(6), 605. <https://doi.org/10.1051/mattech/2025005>
- Javaid, M., Haleem, A., Singh, R. P., Suman, R., & Rab, S. (2021). Role of additive manufacturing applications towards environmental sustainability. *Advanced Industrial*

- and *Engineering Polymer Research*, 4(4), 312–322. <https://doi.org/10.1016/j.aiepr.2021.07.005> 1133 1134
- Ji, K., Zhong, M., & Karma, A. (2025). Phase-field model of alloy solidification far from chemical equilibrium at the solid-liquid interface. *Physical Review Research*, 7(3), 033128. <https://doi.org/10.1103/physrevresearch.7.033128> 1135 1136 1137
- Jiang, J., Xiong, Y., Zhang, Z., & Rosen, D. W. (2022). Machine learning integrated design for additive manufacturing. *Journal of Intelligent Manufacturing*, 33(4), 1073–1086. <https://doi.org/10.1007/s10845-020-01715-6> 1138 1139 1140
- Kaminsky, A. L., Wang, Y., & Pant, K. (2021). An Efficient Batch K-Fold Cross-Validation Voronoi Adaptive Sampling Technique for Global Surrogate Modeling. *Journal of Mechanical Design*, 143(1), 011706. <https://doi.org/10.1115/1.4047155> 1141 1142 1143
- Khatouri, H., Benamara, T., Breitkopf, P., & Demange, J. (2022). Metamodeling techniques for CPU-intensive simulation-based design optimization: A survey. *Advanced Modeling and Simulation in Engineering Sciences*, 9(1), 1. <https://doi.org/10.1186/s40323-022-00214-y> 1144 1145 1146 1147
- Kobayashi, R. (1993). Modeling and numerical simulations of dendritic crystal growth. *Physica D: Nonlinear Phenomena*, 63(3-4), 410–423. [https://doi.org/10.1016/0167-2789\(93\)90120-P](https://doi.org/10.1016/0167-2789(93)90120-P) 1148 1149 1150
- Kurz, W., Rappaz, M., & Trivedi, R. (2021). Progress in modelling solidification microstructures in metals and alloys. Part II: Dendrites from 2001 to 2018. *International Materials Reviews*, 66(1), 30–76. <https://doi.org/10.1080/09506608.2020.1757894> 1151 1152 1153
- Lavinas, Y., Haut, N., Punch, W., Banzhaf, W., & Cussat-Blanc, S. (2024). Adaptive Sampling of Biomedical Images with Cartesian Genetic Programming. In M. Afenzeller, S. M. Winkler, A. V. Kononova, H. Trautmann, T. Tušar, P. Machado & T. Bäck (Eds.), *Parallel Problem Solving from Nature – PPSN XVIII* (pp. 256–272, Vol. 15148). Springer Nature Switzerland. [https://doi.org/10.1007/978-3-031-70055-2\\_16](https://doi.org/10.1007/978-3-031-70055-2_16) 1154 1155 1156 1157 1158 1159
- Lee, H., & Kim, D. (2023). Recent Computational Approaches for Accelerating Dendrite Growth Prediction: A Short Review. *Multiscale Science and Engineering*, 5(3-4), 119–125. <https://doi.org/10.1007/s42493-024-00098-7> 1160 1161 1162
- Li, W., Fang, R., Jiao, J., Vassilakis, G. N., & Zhu, J. (2024). Tutorials: Physics-informed machine learning methods of computing 1D phase-field models. *APL Machine Learning*, 2(3), 031101. <https://doi.org/10.1063/5.0205159> 1163 1164 1165
- Liu, H., Ong, Y.-S., & Cai, J. (2018). A survey of adaptive sampling for global metamodeling in support of simulation-based complex engineering design. *Structural and Multidisciplinary Optimization*, 57(1), 393–416. <https://doi.org/10.1007/s00158-017-1739-8> 1166 1167 1168 1169
- Liu, Z., Ma, Q., Zhang, T., Zhao, S., Gao, X., Sun, T., & Dai, Y. (2025). Quantitative modeling and uncertainty estimation for small-sample LIBS using Gaussian neg- 1170 1171

- ative log-likelihood and monte carlo dropout methods. *Optics & Laser Technology*, 1172  
181, 111720. <https://doi.org/10.1016/j.optlastec.2024.111720> 1173
- Lookman, T., Balachandran, P. V., Xue, D., & Yuan, R. (2019). Active learning in mater- 1174  
ials science with emphasis on adaptive sampling using uncertainties for targeted 1175  
design. *npj Computational Materials*, 5(1), 21. [https://doi.org/10.1038/s41524- 1176](https://doi.org/10.1038/s41524-019-0153-8)  
019-0153-8 1177
- Luo, J., Ma, X., Ji, Y., Li, X., Song, Z., & Lu, W. (2023). Review of machine learning-based 1178  
surrogate models of groundwater contaminant modeling. *Environmental Research*, 1179  
238, 117268. <https://doi.org/10.1016/j.envres.2023.117268> 1180
- Malinin, A., Prokhorenkova, L., & Ustimenko, A. (2021). Uncertainty in gradient boosting 1181  
via ensembles [Poster presentation]. *International Conference on Learning Repres- 1182*  
*entations (ICLR)*. 1183
- Mao, S., Cao, Y., Chen, W., & Sun, D. (2024). An anisotropic lattice Boltzmann - phase 1184  
field model for dendrite growth and movement in rapid solidification of binary 1185  
alloys. *npj Computational Materials*, 10(1), 63. [https://doi.org/10.1038/s41524- 1186](https://doi.org/10.1038/s41524-024-01245-2)  
024-01245-2 1187
- Mao, W., Chen, J., Liu, J., & Liang, X. (2023). Self-Supervised Deep Domain-Adversarial 1188  
Regression Adaptation for Online Remaining Useful Life Prediction of Rolling 1189  
Bearing Under Unknown Working Condition. *IEEE Transactions on Industrial 1190*  
*Informatics*, 19(2), 1227–1237. <https://doi.org/10.1109/TII.2022.3172704> 1191
- McKay, M. D., Beckman, R. J., & Conover, W. J. (1979). A Comparison of Three Methods 1192  
for Selecting Values of Input Variables in the Analysis of Output from a Computer 1193  
Code. *Technometrics*, 21(2), 239. <https://doi.org/10.2307/1268522> 1194
- Migdady, A., Khamayseh, Y., AlZoubi, O., & Yassein, M. B. (2025). An Adaptive Query 1195  
Approach for Extracting Medical Images for Disease Detection Applications. *Ara- 1196*  
*bian Journal for Science and Engineering*, 50(2), 1127–1142. [https://doi.org/10. 1197](https://doi.org/10.1007/s13369-024-09152-w)  
1007/s13369-024-09152-w 1198
- Montes De Oca Zapiain, D., Stewart, J. A., & Dingreville, R. (2021). Accelerating phase- 1199  
field-based microstructure evolution predictions via surrogate models trained by 1200  
machine learning methods. *npj Computational Materials*, 7(1), 3. [https://doi.org/ 1201](https://doi.org/10.1038/s41524-020-00471-8)  
10.1038/s41524-020-00471-8 1202
- Nyamekye, P., Lakshmanan, R., Tepponen, V., & Westman, S. (2024). Sustainability as- 1203  
pects of additive manufacturing: Leveraging resource efficiency via product design 1204  
optimization and laser powder bed fusion. *Heliyon*, 10(1), e23152. [https://doi.org/ 1205](https://doi.org/10.1016/j.heliyon.2023.e23152)  
10.1016/j.heliyon.2023.e23152 1206
- Padarian, J., Minasny, B., & McBratney, A. (2022). Assessing the uncertainty of deep 1207  
learning soil spectral models using Monte Carlo dropout. *Geoderma*, 425, 116063. 1208  
<https://doi.org/10.1016/j.geoderma.2022.116063> 1209
- Palmer, G., Du, S., Politowicz, A., Emory, J. P., Yang, X., Gautam, A., Gupta, G., 1210  
Li, Z., Jacobs, R., & Morgan, D. (2022). Calibration after bootstrap for accurate 1211

- uncertainty quantification in regression models. *npj Computational Materials*, 8(1), 1212–1215. <https://doi.org/10.1038/s41524-022-00794-8>
- Panagiotopoulou, V. C., Stavropoulos, P., & Chryssolouris, G. (2022). A critical review on the environmental impact of manufacturing: A holistic perspective. *The International Journal of Advanced Manufacturing Technology*, 118(1-2), 603–625. <https://doi.org/10.1007/s00170-021-07980-w>
- Park, J., Ryu, I., Ryu, D., & Lee, Y. (2025). An efficient near-optimal Latin hypercube design for large datasets. *Journal of Mechanical Science and Technology*, 39(1), 315–328. <https://doi.org/10.1007/s12206-024-1229-z>
- Peivaste, I., Siboni, N. H., Alahyarizadeh, G., Ghaderi, R., Svendsen, B., Raabe, D., & Mianroodi, J. R. (2022). Machine-learning-based surrogate modeling of microstructure evolution using phase-field. *Computational Materials Science*, 214, 111750. <https://doi.org/10.1016/j.commatsci.2022.111750>
- Rahaman, R., & thiery alexandre, a. (2021). Uncertainty quantification and deep ensembles. In M. Ranzato, A. Beygelzimer, Y. Dauphin, P. Liang & J. W. Vaughan (Eds.), *Advances in neural information processing systems* (pp. 20063–20075, Vol. 34). Curran Associates, Inc.
- Ravutla, S., Bai, A., Realff, M. J., & Boukouvala, F. (2025). Effects of Surrogate Hybridization and Adaptive Sampling for Simulation-Based Optimization. *Industrial & Engineering Chemistry Research*, 64(18), 9228–9251. <https://doi.org/10.1021/acs.iecr.4c03303>
- Samadian, D., Muhit, I. B., & Dawood, N. (2025). Application of Data-Driven Surrogate Models in Structural Engineering: A Literature Review. *Archives of Computational Methods in Engineering*, 32(2), 735–784. <https://doi.org/10.1007/s11831-024-10152-0>
- Seiz, M., Kellner, M., & Nestler, B. (2023). Simulation of dendritic–eutectic growth with the phase-field method. *Acta Materialia*, 254, 118965. <https://doi.org/10.1016/j.actamat.2023.118965>
- Seoh, R. (2020). Qualitative Analysis of Monte Carlo Dropout [Version Number: 1]. <https://doi.org/10.48550/ARXIV.2007.01720>
- Tang, C., & Du, H. (2022). Phase Field Modelling of Dendritic Solidification Under Additive Manufacturing Conditions. *JOM*, 74(8), 2996–3009. <https://doi.org/10.1007/s11837-022-05310-3>
- Tenne, Y. (2015). Initial sampling methods in metamodel-assisted optimization. *Engineering with Computers*, 31(4), 661–680. <https://doi.org/10.1007/s00366-014-0372-z>
- Touret, D., Liu, H., & LLorca, J. (2022). Phase-field modeling of microstructure evolution: Recent applications, perspectives and challenges. *Progress in Materials Science*, 123, 100810. <https://doi.org/10.1016/j.pmatsci.2021.100810>

- Tyralis, H., & Papacharalampous, G. (2024). A review of predictive uncertainty estimation with machine learning. *Artificial Intelligence Review*, 57(4), 94. <https://doi.org/10.1007/s10462-023-10698-8>
- Usman, M., Ahmad, I., Ahsan, M., & Caliskan, H. (2024). Prediction and optimization of emissions in cement manufacturing plant under uncertainty by using artificial intelligence-based surrogate modeling. *Environment, Development and Sustainability*. <https://doi.org/10.1007/s10668-024-05068-5>
- Vasylenko, A., Gamon, J., Duff, B. B., Gusev, V. V., Daniels, L. M., Zanella, M., Shin, J. F., Sharp, P. M., Morscher, A., Chen, R., Neale, A. R., Hardwick, L. J., Claridge, J. B., Blanc, F., Gaultois, M. W., Dyer, M. S., & Rosseinsky, M. J. (2021). Element selection for crystalline inorganic solid discovery guided by unsupervised machine learning of experimentally explored chemistry. *Nature Communications*, 12(1), 5561. <https://doi.org/10.1038/s41467-021-25343-7>
- Viana, F. A. C., Gogu, C., & Goel, T. (2021). Surrogate modeling: Tricks that endured the test of time and some recent developments. *Structural and Multidisciplinary Optimization*, 64(5), 2881–2908. <https://doi.org/10.1007/s00158-021-03001-2>
- Viardin, A., Nöth, K., Pickmann, C., & Sturz, L. (2025). Automatic Detection of Dendritic Microstructure Using Computer Vision Deep Learning Models Trained with Phase Field Simulations. *Integrating Materials and Manufacturing Innovation*, 14(1), 89–105. <https://doi.org/10.1007/s40192-025-00392-8>
- Wang, J., Li, Y., Gao, R. X., & Zhang, F. (2022). Hybrid physics-based and data-driven models for smart manufacturing: Modelling, simulation, and explainability. *Journal of Manufacturing Systems*, 63, 381–391. <https://doi.org/10.1016/j.jmsy.2022.04.004>
- Wang, Q., Li, Y., & Li, R. (2024). Ecological footprints, carbon emissions, and energy transitions: The impact of artificial intelligence (ai). *Humanities and Social Sciences Communications*, 11(1), 1–18.
- Wang, S., Lv, L., Du, L., & Song, X. (2019). An improved lhs approach for constrained design space based on successive local enumeration algorithm. *2019 IEEE 9th Annual International Conference on CYBER Technology in Automation, Control, and Intelligent Systems (CYBER)*, 896–899. <https://doi.org/10.1109/CYBER46603.2019.9066677>
- Würth, T., Krauß, C., Zimmerling, C., & Kärger, L. (2023). Physics-informed neural networks for data-free surrogate modelling and engineering optimization – An example from composite manufacturing. *Materials & Design*, 231, 112034. <https://doi.org/10.1016/j.matdes.2023.112034>
- Xiao, Q., Wang, J., Jiang, B., Yang, W., & Yang, X. (2022). Multi-objective optimization of squirrel cage fan for range hood based on Kriging model. *Proceedings of the Institution of Mechanical Engineers, Part C: Journal of Mechanical Engineering Science*, 236(1), 219–232. <https://doi.org/10.1177/0954406221995863>

- Xue, D., Li, Y., Zhang, H., Tong, X., Gao, B., & Yu, J. (2024). Reliability-based robust optimization design for tolerance of aerospace thin-walled components based on surrogate model. *Advanced Engineering Informatics*, 62, 102754. <https://doi.org/10.1016/j.aei.2024.102754>
- Yan, H., Yu, H., Zhu, S., Yin, Y., & Guo, L. (2024). Machine learning based framework for rapid forecasting of the crack propagation. *Engineering Fracture Mechanics*, 307, 110278. <https://doi.org/10.1016/j.engfracmech.2024.110278>
- Yu, Y., Wang, L., Zhou, J., Li, H., Li, Y., Yan, W., & Lin, F. (2022). Impact of fluid flow on the dendrite growth and the formation of new grains in additive manufacturing. *Additive Manufacturing*, 55, 102832. <https://doi.org/10.1016/j.addma.2022.102832>
- Zeevi, T., Venkataraman, R., Staib, L. H., & Onofrey, J. A. (2024). Monte-Carlo Frequency Dropout for Predictive Uncertainty Estimation in Deep Learning. *2024 IEEE International Symposium on Biomedical Imaging (ISBI)*, 1–5. <https://doi.org/10.1109/ISBI56570.2024.10635511>
- Zeng, H.-b., Ai, X.-g., Chen, M., Guan, R., Chao, Y.-f., & Zhang, J.-c. (2024). Phase-field simulation study on dendritic growth behavior during bilateral directional solidification. *Materials Today Communications*, 40, 109618. <https://doi.org/10.1016/j.mtcomm.2024.109618>